234

ELSEVIER

Materials Science and Engineering A000 (2001) 000–000

MATERIALS SCIENCE & ENGINEERING A

www.elsevier.com/locate/msea

Constitutive description of dynamic deformation: physically-based mechanisms

M.A. Meyers [a,*], D.J. Benson [a], O. Vöhringer [b], B.K. Kad [a], Q. Xue [a], H.-H. Fu [a], Y.-J. Chen [a]

[a] *Department of Mechanical and Aerospace Engineering, University of California, La Jolla, CA, USA*
[b] *Department of Mechanical Engineering, Institute for Materials Science I, University of Karlsruhe (TH), Karlsruhe, Germany*

Abstract

The response of metals to high-strain-rate deformation is successfully described by physically-based mechanisms which incorporate dislocation dynamics, twinning, displacive (martensitic) phase transformations, grain-size, stacking fault, and solution hardening effects. Several constitutive equations for slip have emerged, the most notable being the Zerilli–Armstrong and MTS. They are based on Becker's and Seeger's concepts of dislocations overcoming obstacles through thermal activation. This approach is illustrated for tantalum and it is shown that this highly ductile metal can exhibit shear localization under low temperature and high-strain-rate deformation, as predicted from the Zerilli–Armstrong equation. A constitutive equation is also developed for deformation twinning. The temperature and strain-rate sensitivity for twinning are lower than for slip; on the other hand, its Hall–Petch slope is higher. Thus, the strain rate affects the dominating deformation mechanisms in a significant manner, which can be quantitatively described. Through this constitutive equation it is possible to define a twinning domain in the Weertman–Ashby plot; this is illustrated for titanium. A constitutive description developed earlier and incorporating the grain-size dependence of yield stress is summarized and its extension to the nanocrystalline range is implemented. Computational simulations enable the prediction of work hardening as a function of grain size; the response of polycrystals is successfully modeled for the 50 nm–100 m range. The results of shock compression experiments at pulse durations of 3–10 ns (this is two–three orders less than gas-gun experiments) are presented. They prove that the defect structure is generated at the shock front; the substructures observed are similar to the ones at much larger durations. A mechanism for dislocation generation is presented, providing a constitutive description of plastic deformation. The dislocation densities are calculated which are in agreement with observations. The threshold stress for deformation twinning in shock compression is calculated from the constitutive equations for slip, twinning, and the Swegle–Grady relationship.

Keywords: High-strain-rate deformation; Metals; Physically-based mechanisms

1. Introduction

Crystalline metals can deform plastically by one (or more) of the following mechanisms: slip, twinning, displacive transformations, or diffusional creep processes. Dislocations play a pivotal role in the first three mechanisms, since they are the units of plastic shear. In creep, a number of mechanisms involve dislocations, either directly or through pipe diffusion. Grain-boundary sliding and Coble creep may also involve grain-boundary dislocations.

The current framework for understanding and quantitatively predicting the kinetics of the four mechanisms of plastic deformation rests on the theory of thermally activated processes. John Dorn, to whom this symposium is dedicated, applied this theory to creep and developed a quantitative, physically based underpinning for the processes involved. The Sherby–Dorn [1] equation for predicting the stress–rupture life and the Mukherjee–Bird–Dorn [2] equation for creep are two cornerstones of our contemporary treatment of high-temperature deformation and creep.

The objective of this paper was to present, in a synoptic fashion, the research carried out by the authors over the past 5 years, with emphasis on high-strain-rate deformation. For clarity, this contribution is

* Corresponding author. Tel.: +1-858-5344719; fax: +1-858-5345698.
E-mail address: mameyers@mae.ucsd.edu (M.A. Meyers).

0921-5093/01/$ - see front matter
PII: S0921-5093(01)01131-5

divided into four parts: (a) constitutive description of plastic deformation by slip; (b) the slip–twinning transition; (c) grain-size effects; and (d) the upper limit: shock compression. Thermal activation is central to these processes and is briefly reviewed first.

2. Constitutive description of plastic deformation by slip

The seminal work by Becker [3] and Seeger [4–7] provides the underpinning for the contemporary constitutive description of plastic deformation of metals. The basic concepts of Becker and Seeger were further developed by Conrad [8–10], Krausz and Eyring [11], Ono [12], Vöhringer [13], Kocks and co-workers [14,15], Klepaczco [16,17], and Zerilli and Armstrong [18,19]. There is a considerable number of assumptions underlying the current constitutive models. We present below a summary of the principal elements of this approach. Greater detail is provided elsewhere [20,21]. The fundamental equation upon which these constitutive descriptions rests is the commonly referred to 'Arrhenius' equation. It is instructive to analyze it into some detail, since it is seldom if ever presented; the reader is simply compelled to accept that dislocations obey this chemical reaction relationship.

In 1889 Arrhenius observed that there is an 'activated state' intermediate between reactants and products. He suggested that the reaction rate was controlled by a rate constant k' given by

$$k' = A \exp\left(\frac{-\Delta E_e}{kT}\right) \tag{1}$$

where A is a frequency factor and ΔE_e is the activation energy for the process. This equation was based on van't Hoff's equation describing the effect of the temperature on the equilibrium constant for reactions.

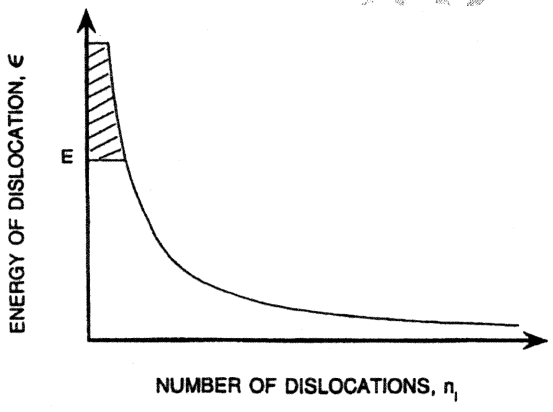

Fig. 1. Boltzmann's distribution of energy states applied to dislocations.

However, the rigorous proof for this equation is rooted in statistical mechanics and in Boltzmann statistics. The movement of a dislocation requires it to pass through an 'activated state'. Quantum-mechanical calculations are required to calculate the exact shape of the potential-energy barriers facing a dislocation, and many shapes were proposed. Current models use the shape that provides the best fit of macroscopic mechanical properties. We will present here, in a simplified manner, how these concepts are derived. The Boltzmann law of energy distribution is the most important equation of statistical mechanics. The basic premise is that energy is quantized and that the smallest quantity is $h\nu$, where h is Planck's constant and ν is the frequency of vibration of oscillator.

We consider N dislocations which are arrested by obstacles; each dislocation is considered to be an oscillator. The dislocations have different energy levels, and the energy levels are quantized, i.e. they are discrete. Each level is filled up with a specific number of dislocations n_i. It can be shown that the distribution of n_i dislocations, at energy levels ε_i, is an exponential function that is represented in Fig. 1 and is given by

$$n_i = Ae^{-\beta\varepsilon_i} \tag{2}$$

This is the Boltzmann distribution. The terms A and β are parameters that express the distribution.

The probability that a dislocation has an energy equal to or greater than E (the hatched region in Fig. 1) is given by

$$p_E = \frac{A\int_E^\infty e^{-\beta\varepsilon_i}\,d\varepsilon_i}{A\int_0^\infty e^{-\beta\varepsilon_i}\,d\varepsilon_i} = e^{-\beta E} \tag{3}$$

We now introduce the fundamental postulate of statistical mechanics.

$$S = k \ln W \tag{4}$$

where S is the entropy, k is Boltzmann's constant, and W is the number of ways in which N objects (in our case, dislocations) can be arranged. If we consider that dislocations can occupy i energy levels, and that all n_i dislocations at a level i are undistinguishable, we have:

$$\frac{S}{k} = \ln\frac{N!}{n_1!n_2!n_3!\ldots} = \ln\frac{N!}{\Pi n_i!} \tag{5}$$

Using Stirling's approximation:

$$\ln W = \frac{S}{k} = N\ln N - \sum n_i \ln n_i = N\ln N - \sum n_i \ln n_i \tag{6}$$

Using Eqs. (2) and (3) and thermodynamic relationships (see Meyers [21]), we show that $\beta = 1/kT$ and arrive at the probability that a dislocation has an energy greater than E:

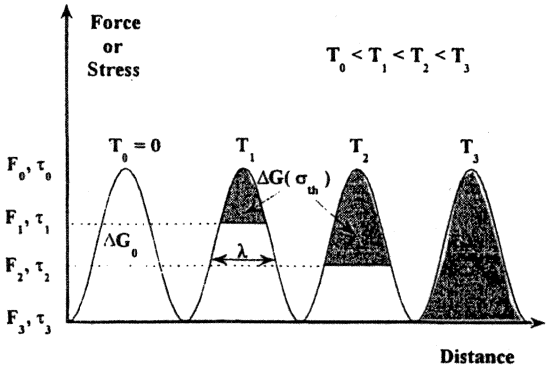

Fig. 2. Schematic of a dislocation overcoming barriers with the assistance of thermal energy.

$$p_E = e^{-E/kT} \tag{7}$$

We assume that the dislocation will overcome the obstacle when its energy exceeds the height of the obstacle, E. The PV (pressure multiplied by volume) term is small in condensed solids and therefore the internal energy E and enthalpy ΔH are approximately equal. Thus:

$$p = \exp\left(-\frac{\Delta H}{kT}\right) = \exp\left(-\frac{\Delta G - TS}{kT}\right)$$
$$= \exp -\frac{\Delta G}{kT} \exp -\frac{S}{k} = A \exp\left(-\frac{\Delta G}{kT}\right) \tag{8}$$

The term $\exp(\Delta S/k)$ is designated A.

All the modern constitutive equations are really based on this expression. Basically, it says that, given a barrier of a height ΔG, the probability that an entity (in our case, a dislocation) will jump over the barrier is p. As the temperature goes up, the probability increases because thermal energy will provide the 'kick' that allows the entity to jump over the barrier. The frequency of successful jumps is related to the probability by:

$$P = v_1/v_0 \tag{9}$$

where v_0 is the vibrational frequency of the dislocation (considerably lower then the vibrational frequency of an atom) and v_1 is the frequency of successful jumps. So:

$$v_1 = v_0 A \exp\left(-\frac{\Delta G}{kT}\right) \tag{10}$$

The Orowan equation (with an orientation factor M) can now be applied to relate the strain to the movement of the dislocations:

$$\frac{d\gamma}{dt} = \frac{1}{M} \rho b \frac{\Delta l}{\Delta t} \tag{11}$$

where ρ is the dislocation density, b the Burgers vector, Δl the distance between dislocation barriers, and M an orientation parameter. The total transit time of a dislocation is equal to the sum of the waiting time (at an obstacle) and the travel time between obstacles. We now assume that the transit time is negligible. This waiting time, $\Delta t = t_w$, is the inverse of the successful jump frequency, v_1. When Eq. (10) is substituted in Eq. (11), the strain rate becomes

$$\frac{d\gamma}{dt} = \frac{v_0 \rho b \Delta l A}{M\gamma} \exp\left[\frac{-\Delta G}{kT}\right] \tag{12}$$

The terms before the exponential term can be grouped together and called $\dot{\gamma}_0$:

$$\dot{\gamma} = \dot{\gamma}_0 \exp\left[\frac{-\Delta G}{kT}\right] \tag{13}$$

By solving for ΔG, one can obtain the equation

$$\Delta G = kT \ln \frac{\dot{\gamma}}{\dot{\gamma}} \tag{14}$$

Remember that there are different barrier shapes that can be considered and one would assume that different shapes would give different constitutive equations. Fig. 2 shows a generic barrier and the assistance of thermal energy as the temperature is increased from 0 K. Whereas Seeger initially proposed a rectangular barrier, Ono [12] compared square, triangular, parabolic, exponential, etc. Kocks et al. [14] proposed a generalized equation for these shapes with two parameters, p and q. They said that their equation could fit any shape. Their equation is of the form:

$$\Delta G = \Delta G_0 \left[1 - \left(\frac{\tau}{\tau_0}\right)^p\right]^q \tag{15}$$

By equating Eqs. (14) and (15), we arrive at a general constitutive equation relating stress, strain rate, and temperature. The stress is often decomposed into an internal component due to long-range barriers, s_G, that cannot be assisted by thermal energy, and an effective component, due to short-range barriers, s*, which is thermally assisted.

In order to understand quantitatively the deformation behavior of metals, a constitutive description is needed; the Zerilli–Armstrong model is used here for illustration purposes. It has the advantage of being simple and readily implementable, while capturing the essential physical phenomena. Zerilli and Armstrong [18,19] correctly pointed out that the activation volumes in BCC and FCC metals are quite different, in view of the different rate controlling mechanisms: in FCC metals, the cutting of dislocations by forests is the principal mechanism, whereas the overcoming of Peierls–Nabarro barriers is the principal mechanism in BCC metals. In FCC metals, the activation volume decreases with plastic strain because of the increase in

dislocation density; in BCC metals, it is constant. Thus, the constitutive equations take different forms. Zerilli and Armstrong [18] developed a constitutive equation for BCC metals and applied it to tantalum, based on the results by Bechtold [22], Hoge and Mukherjee [23], and Mitchell and Spitzig [24]. The constitutive equation is given below:

$$\sigma = \sigma_G + B_0 e^{-(\beta_0 - \beta_1 \ln \dot{\varepsilon})T} + K\varepsilon^n + kd^{-1/2} \quad (16)$$

σ_G is the athermal portion of the stress, n the work hardening, d the grain size, and β_0, β_1, B_0, K, and k are parameters. Tantalum was also used in our research [25,26]. Because of the different chemistry and processing history of material used in our research, a new set of parameters for this model had to be determined from experiments. The thermal and strain rate responses were experimentally determined and are given in Table 1, along with the data of Hoge and Mukherjee [23]. To minimize the deviation at high strain rates, the strain hardening parameters were determined at a strain rate of 3500/s and room temperature.

At high strain rates, there are interrupted tests described by Meyers et al. [25] which provide a quasi-isothermal curve, from which the adiabatic curve can be obtained. These interrupted experiments were introduced by Wittman et al. [27]. Fig. 3 presents the experimental results and Z–A predictions. The continuous lines in Fig. 3 a and b represent the application of the Zerilli–Armstrong equation to the various temperatures and strain rates of interest. Fig. 3c shows the stress strain curves predicted from the Zerilli–Armstrong model under both isothermal and adiabatic conditions at various temperatures and 3500/s. The adiabatic temperature of the plastically deformed specimen was estimated by assuming the conversion of 90% plastic work into heat. The adiabatic curves go through a maximum beyond which the material softens. The instability strain is taken as the maximum in the adiabatic stress–strain curve and is mathematically expressed by:

$$\frac{d\sigma}{d\varepsilon} = -B(\beta_0 - \beta_1 \ln \dot{\varepsilon}) \frac{dT}{d\varepsilon} e^{-(\beta_0 - \beta_1 \ln \dot{\varepsilon})T} + Kn\varepsilon^{n-1} = 0 \quad (17)$$

This equation has to be solved numerically. The instability strain increases with temperature, as shown in Fig. 3c; this is the direct result of the interplay among the various parameters. In this particular case, both the higher thermal softening rate ($d\sigma/dT$) and lower heat capacity, contribute significantly to a lower instability strain at low temperatures. It also decreases with increasing strain rate at 298 K, as shown by Fig. 3d. The Z–A predictions are corroborated by experiment. Fig. 4 shows the cross-section of a specimen tested at a strain of −0.6 in a Kolsky–Hopkinson bar, at a strain rate of 5500 s^{-1} and temperature of 77 K. There is clear and irrefutable evidence of shear localization, in accordance with the predictions of Fig. 3 c and d. The predicted strain for instability (a requirement for localization) decreases with increasing strain rate and decreasing temperature. It is concluded that physically-based constitutive equations are essential components of modern research on the mechanical behavior of materials. The implementation of these equations into codes, such as DYNA-2D, in the example shown in Fig. 5, illustrates the realistic effects obtained. The break-up of the material removed by the cutting tools into discrete chips, due to adiabatic heating and shear localization, is clearly shown.

At low temperatures and high strain rates, the Zerilli–Armstrong model prediction of yield stress is higher than the experimental results; this is indicated by an arrow in Fig. 3a. This is attributed to the change of the predominant deformation mechanism from dislocation slip to twinning at low temperatures and high strain rates. Mechanical twinning was observed in high strain rate testing at both 77 and 190 K. The current constitutive models do not take the slip–twinning transition into effect, and Zerilli and Armstrong [28] have recently discussed the importance of including twinning into the constitutive response. The mechanical twins formed at low temperatures are significantly different from shock-induced twins reported by Murr et al. [29] in the same tantalum. The low temperature twins are usually larger in size and have a lower frequency in occurrence. In shock compression, the high stress (45 GPa) provided a large driving force for mechanical twinning which results in a high nucleation rate. The size of twins was limited by the large number of twins themselves (twin–twin intersections) and by the limited time of pulse duration (1.8 μs); in contrast, the duration of the stress pulse in the Hopkinson–Kolsky bar is ~100 μs.

Table 1
Parameters of Zerilli–Armstrong equation for tantalum

	$\sigma_G + kd^{-1/2}$	B_0	β_0	β_1	K	n
Chen et al. [25,26]	122	1330	0.00525	0.000308	197	0.5
Hoge-Mukherjee [23]	30	1125	0.00535	0.00327	310	0.44

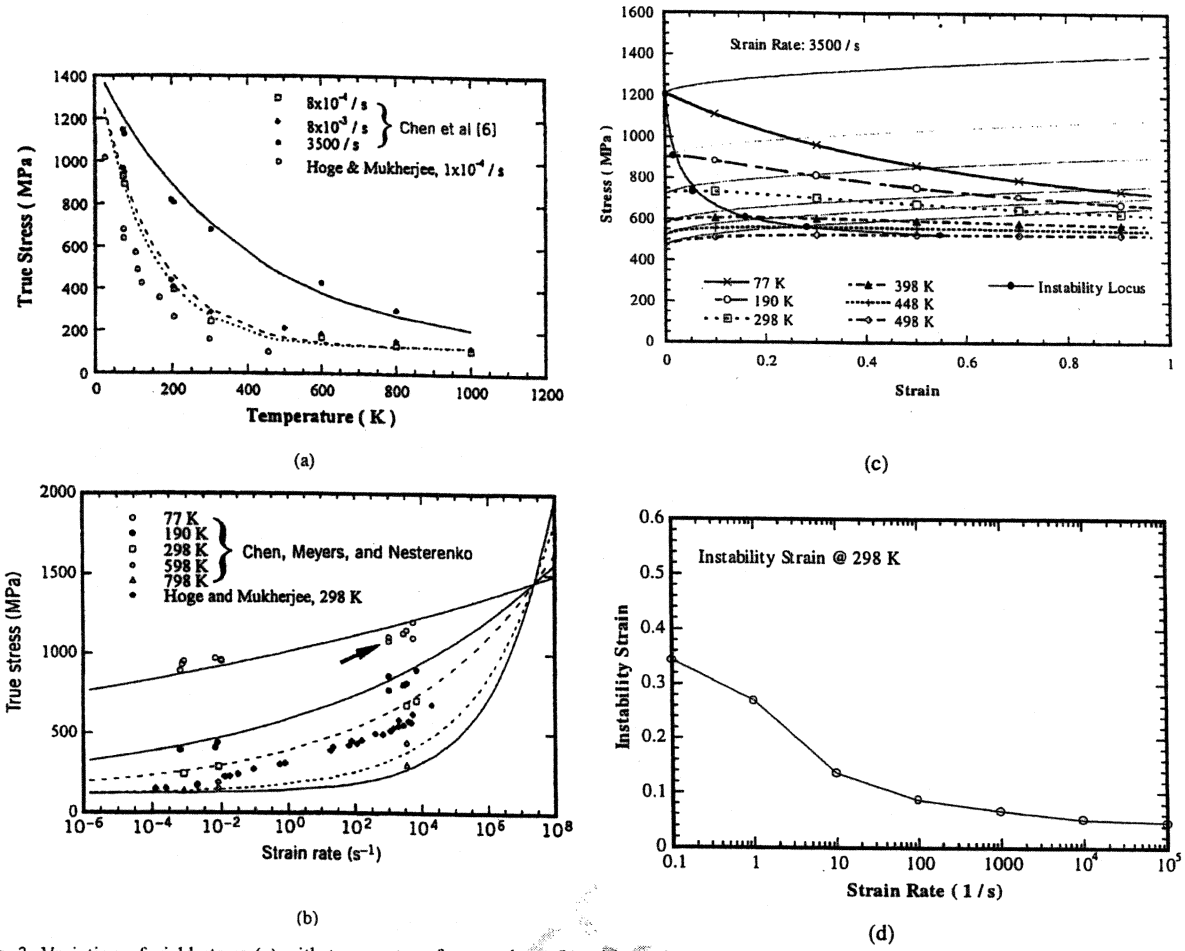

Fig. 3. Variation of yield stress (a) with temperature for tantalum; (b) with strain rate for tantalum; (c) isothermal and adiabatic stress–strain curves predicted from Zerilli–Armstrong equation with instability points marked; (d) instability strain as a function of strain rate (assuming adiabaticity).

3. The slip–twinning transition

A constitutive approach was recently developed [31,32] that predicts the critical stress for twinning as a function of external (temperature, strain rate) and internal (grain size, stacking-fault energy) parameters. Plastic deformation by slip and twinning being competitive mechanisms (it is, of course, recognized that twinning requires dislocation activity), the twinning constitutive relationship is equated to a slip relationship based on the plastic flow by thermally assisted movement of dislocations over obstacles; this leads to the successful prediction of the slip–twinning transition. Using an Eshelby-type analysis, the critical twin nucleus size and twinning stress were correlated to the twin-boundary energy, which is directly related to the stacking-fault energy for FCC metals [32]. It will be shown here that the constitutive description of the slip–twinning transition can be incorporated into the Weertman–Ashby deformation mechanism maps, thereby enabling the introduction of a twinning domain; this is illustrated for titanium with a grain size of 100 μm. A summary of the salient aspects of this work is presented below.

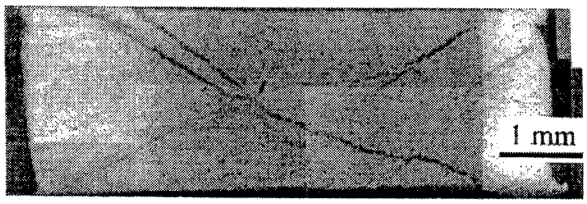

Fig. 4. Tantalum specimen tested in compression to a total strain of −0.6 at 77 K and 5500 s^{-1}.

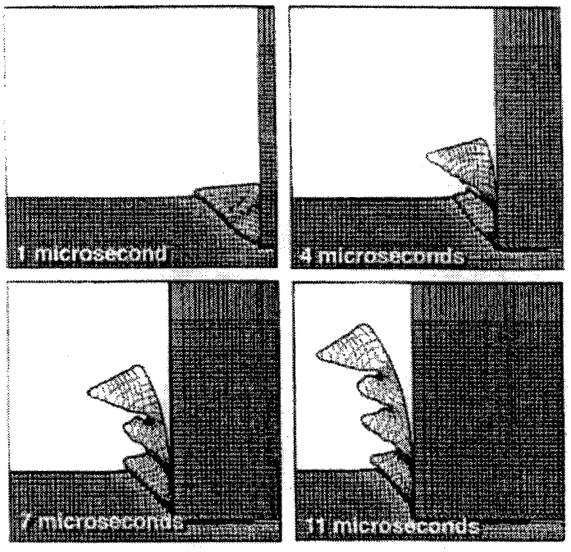

Fig. 5. Computational prediction of chip formation through adiabatic shear localization in machining.

3.1. *Effects of temperature, grain size, stacking-fault energy, and texture*

Fig. 6 shows a compilation of twinning stresses versus temperature for a number of metals (both mono and polycrystals). The striking aspect is that there seems to be a critical stress that is temperature-insensitive. This issue has been debated in the literature, and there are diverging results. A large scatter has been observed in single crystals. This could, however, be attributed to stress concentration sites other than pile ups (surface notches, internal flaws, etc.). Hence, a distribution of twinning stresses, similar to a Weibull distribution for ceramic strength, would be expected. There are also reports of gradual decrease in the twinning stresses with increasing temperature for FCC metals. Christian and Mahajan [32] discuss this topic in detail. Mahajan and Williams [33] suggested that BCC metals have a negative dependence of twinning stress on temperature, while FCC metals have a slightly positive temperature sensitivity. However, Reed-Hill [34,35] concluded that whenever the deformation proceeds primarily by twinning, the flow stress tends to have a positive temperature dependence and a negative strain rate dependence. For the purposes of the subsequent calculations, it will be assumed that there is a critical stress for twinning that is either temperature-independent or has a very low temperature dependence. For the FCC and HCP structures the strain rate dependence of the twinning stress has not received the same degree of attention, and the only account in which the strain rate is varied over a very broad range is to the authors' knowledge the work of Harding [36,37] on monocrystalline iron, shown in Fig. 6. The twinning shear stress at $10^3\ s^{-1}$ is approximately 220 MPa, whereas it is equal to 170 MPa at $10^{-3}\ s^{-1}$. This result is used in a simple constitutive equation for twinning presented later, but additional experiments are clearly necessary to establish the strain rate dependence.

Another highly unique characteristic of twinning, first pointed out by Armstrong and Worthington [38], is the larger grain size dependence of the twinning stress, as compared with the slip stress. For most cases, a Hall–Petch relationship is obeyed, but with a slope, k_T, that is higher than the one for slip, k_S:

$$\sigma_T = \sigma_{0T} + k_T d^{-1/2} \tag{18}$$

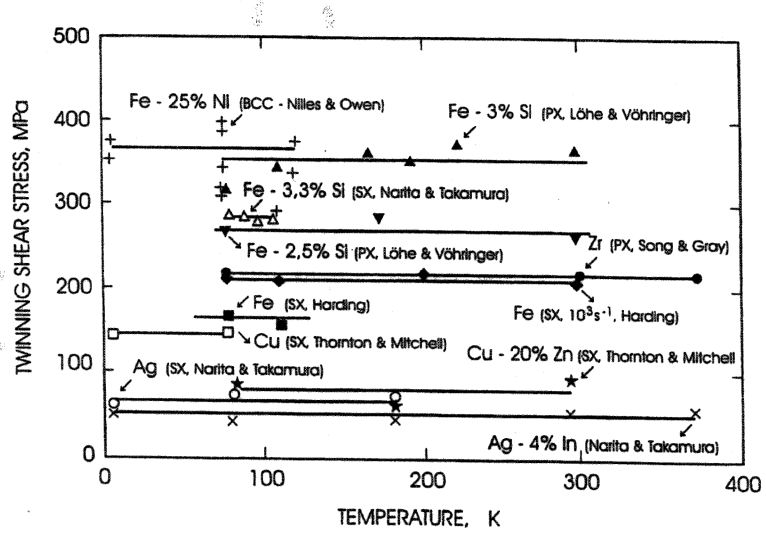

Fig. 6. Twinning stress as a function of temperature for a number of metals (both mono and polycrystals).

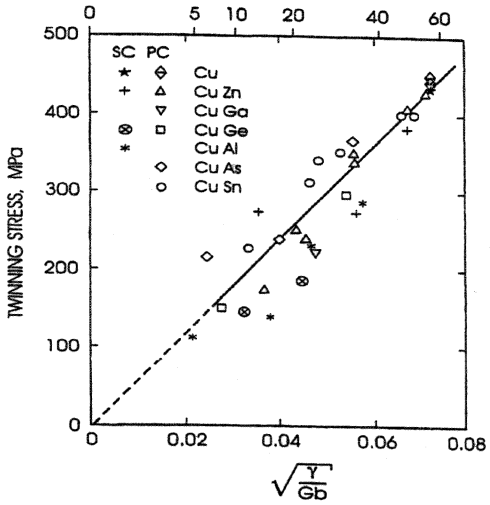

Fig. 7. Twinning stress as a function of stacking fault energy for copper and copper solid solutions.

The Hall–Petch slope for twinning found by Vöhringer [39,40] significantly exceeds the one for slip for copper; $k_T = 0.7$ MPa $m^{1/2}$ and $k_S \cong 0.35$ MPa $m^{1/2}$. Table 1 is a compilation of data for BCC, FCC, and HCP metals from a number of sources. The reason for this difference is not fully understood, but Armstrong and Worthington [38] suggest that twinning is associated with microplasticity, i.e. dislocation activity occurring before the onset of generalized plastic deformation, whereas the yield stress is associated with generalized plastic deformation. It is very plausible that microplasticity and overall deformation are controlled by different mechanisms, i.e. elastic anisotropy, incompatibility stresses, and barriers to slip.

It is well known that the twinning stress increases with increasing stacking-fault energy. This is true mostly for FCC metals, where the classic plot by Venables [41] shows this effect very clearly. Fig. 7 shows a compilation of results by Venables [41] and Vöhringer [39,40]. The twinning stress for a number of copper alloys is shown to vary with the square root of the stacking-fault energy, γ_{SF}. Recently, El-Danaf et al. [43] and Asgari et al. [42] reanalyzed the effect of stacking-fault energy on the twinning stress.

Gray et al. [44] have shown that texture is especially important in low-symmetry metals. They demonstrated this effect for Ti and Zr. There is an intrinsic difference between slip and twinning that leads to significant differences in the effect of texture. A dislocation moves in opposite senses (one direction contains two senses) when the applied stress sign is reversed; one can consider the critical resolved shear stress to be independent of the sense of motion of a dislocation. A twin, on the other hand, has a definite twin plane and a twinning sense (a well defined direction of motion). In the absence of texture these differences do not manifest themselves. The twinning and slip stresses are the same in compression and tension. In the presence of texture, however, the twinning stresses in compression and tension are different. The analysis presented here applies only to an isotropic (untextured) polycrystalline aggregate.

3.2. Constitutive description

Meyers et al. [30] and Meyers and Vöhringer [31] arrive at a relationship between twinning stress, temperature, and strain rate, starting with the basic Johnston–Gilman equation. This equation is:

$$\sigma_{0T} = M\left(\frac{n^* lE}{2A}\right)^{1/m+1} \dot{\varepsilon}^{1/m+1} e^{Q/(m+1)RT} = K\dot{\varepsilon}^{1/m+1} e^{Q/(m+1)RT} \quad (19)$$

where parameter m is the exponent in the Johnston–Gilman [45] dislocation dynamics equation. This equation is applied to iron in order to establish the strain rate and temperature dependence of twinning. The experimental results of Stein and Low [46] for Fe–3 wt. Si are used for m ($=36$) and Q ($=51.66$ kJ/mol). The activation energy was obtained by plotting the dislocation velocity (at a constant stress) as a function of $1/T$. The term $K = M(n^* lE/2A)^{1/(m+1)}$ is obtained by fitting Eq. (19) to the experimental results reported by Harding [36,37] for the twinning stress. The following equation is obtained:

$$\sigma(\text{in MPa}) = 380\dot{\varepsilon}^{1/37} e^{0.17/T} \quad (20)$$

$$\sigma = \sigma_G + C_1 \exp(-C_3 T + C_4 T \ln \dot{\varepsilon}) \quad (21)$$

It can be seen that the slip and twinning response differ drastically. Twinning exhibits a very weak temperature dependence; below 20 K, the Johnston–Gilman equation breaks down, because the stress goes to infinity. We now establish the critical condition: the onset of twinning occurs when the slip stress, σ_S, becomes equal to the twinning stress, σ_T:

$$\sigma_T = \sigma_Y \quad (22)$$

This rationale will be applied to typical metals representative of the three crystalline systems of greatest importance for metals: Fe (BCC), Cu (FCC), Ti (HCP). It should be noted that no attempt was made, at the present stage, to compare the calculated slip–twinning transitions with experimental results on the initiation.

3.2.1. Iron (BCC)

The constitutive equations given in Eqs. (19) and (21) are applied to Eq. (22), with the addition of the Hall–Petch terms for slip and twinning, k_S and k_T, respectively. This leads to

$$\sigma_G + K\dot{\varepsilon}^{1/m+1} e^{Q/(m+1)RT} - C_1 e^{-(C_3 - C_4 \ln \dot{\varepsilon})T} + (k_T - k_S)d^{-1/2} = 0 \quad (23)$$

Fig. 8a shows the slip–twinning transition for different grain sizes. This plot, in the temperature–strain rate space, defines two domains: slip and twinning. The lines represent the boundaries between these domains. The effect of grain size is clearly seen and is due to the fact that $k_T > k_S$. The values for k_T and k_S are equal to 124 and 20 MPa $m^{1/2}$, respectively. This explains why the twinning domain for monocrystalline iron is much larger than for polycrystalline iron. An increase in grain size predisposes iron to twinning.

3.2.2. Copper (FCC)

It was not possible to apply the constitutive equation [Eq. (19)] for twinning to copper. Therefore, it was decided to simply use the twinning stress determined experimentally. Thornton and Mitchell [47] report a shear twinning stress for monocrystalline copper of 150 MPa and this value is taken. The Hall–Petch slope for twinning was obtained by Vöhringer [39,40,48]; it is equal to 0.68 MPa $m^{1/2}$. The slip response was modeled by the Zerilli–Armstrong equation for FCC metals. The equation is:

$$\sigma = \sigma_G + C_2 \varepsilon^{n} \exp(-C_3 T + C_4 \ln \dot{\varepsilon}) + k_S d^{-1/2} \quad (24)$$

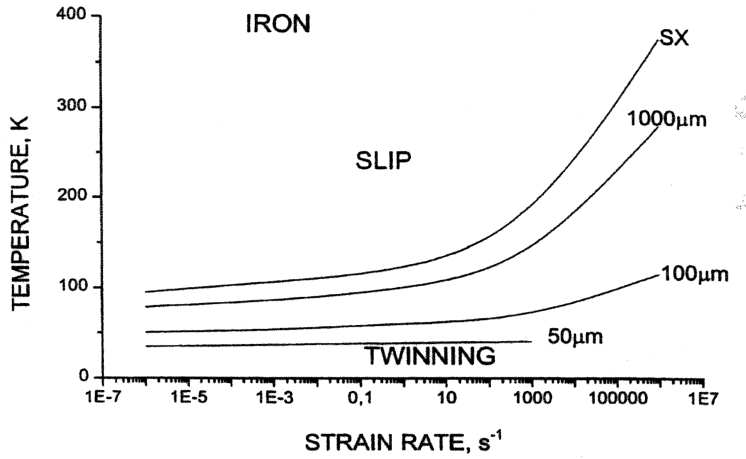

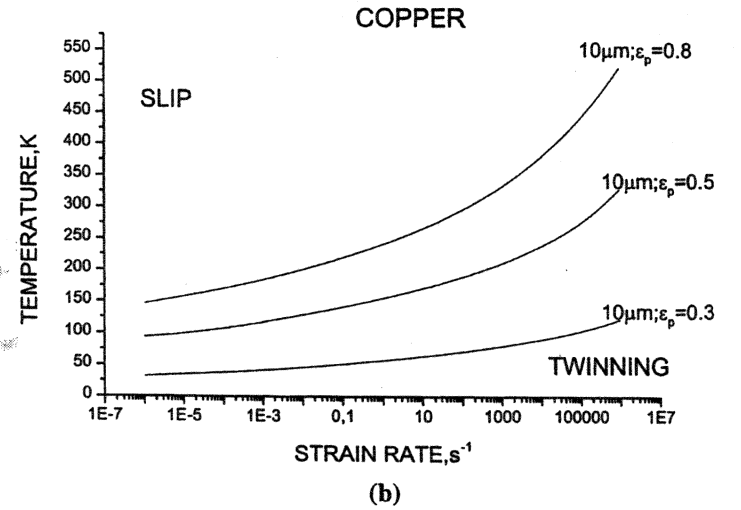

Fig. 8. (a) Calculated slip–twinning transition for iron of different grain sizes. (b) Calculated slip–twinning transition for copper (d = 10 μm), at different plastic strain levels: 0.3, 0.5, 0.8.

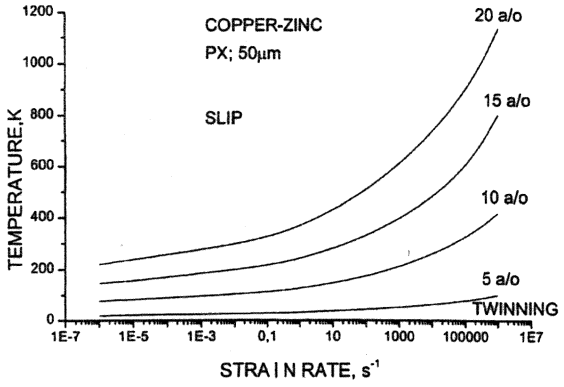

Fig. 9. (a) Calculated slip–twinning transition for polycrystal Cu–Zn brasses with grain size 50 μm; (b) calculated slip–twinning transition for titanium with different grain sizes.

The slip–twinning transition as a function of grain size was also established [30,31]. The effect of grain size is dramatic and it influences the occurrence of twinning in a significant way. The effect of plastic strain is clearly seen in the slip–twinning transition plot of Fig. 8b. These calculations were done for a constant grain size of 10 μm and strains of 0.3, 0.5, and 0.8. A plastic strain of 0.3 is necessary to initiate twinning. At ambient temperature, a strain rate of 5×10^3 s^{-1} and strain of 0.8 are required to produce twinning.

3.2.3. Titanium (HCP)

Zerilli and Armstrong [48,49] have demonstrated that the constitutive response of BCC metals can represent the behavior of titanium, with a few modifications to incorporate the decrease in work hardening rate as the temperature is increased. The equation is:

$$\sigma = \sigma_G + C_1\left(\frac{\dot{\varepsilon}_0}{\dot{\varepsilon}}\right)^{-C_3T} + \frac{C_2}{e^{-C_4T}}\varepsilon^{n} + k_S d^{-1/2} \quad (25)$$

The term e^{-C_4T} decreases the work hardening as T increases. The twinning stress is simply represented by:

$$\sigma_T = \sigma_{T0} + k_T d^{-1/2} \quad (26)$$

Gray [50] reported a greater propensity for mechanical twinning of large grain sized (240 μm) than smaller grain sized (20 μm) Ti in dynamic testing, in agreement with the assumption that $k_T > k_S$. Conrad et al. [53] report similar effects. The critical twinning stress is reported by Zerilli and Armstrong [51]. It is known that interstitials have a major effect on the mechanical response of Ti [52]. For instance, the yield stress of Ti at RT increases from 150 to 600 MPa, when the oxygen equivalent (O + N + C) percentage is increased from 0.1 to 1.0%. This effect is more important than the grain size, where the yield stress increases from 450 to 600 MPa when the grain size is decreased from 1.5 mm to 1.5 μm (for 1%Oeq.). The Hall Petch slope for slip was obtained by Okazaki and Conrad [54] and was found to be relatively insensitive to interstitial content. Conrad et al. [53] report twinning shear stresses in monocrystalline Ti, for $(10\bar{1}2)$ and $(11\bar{2}1)$ planes, between 420 and 380 MPa, respectively. These twinning stresses decrease with decreasing temperature. Taking a value of 800 MPa for the normal stresses, the slip–twinning transition was estimated for grain sizes of 3, 10, and 100 μm. These values are given in Fig. 9a. It should be noted that the calculations were carried out for Marz titanium, with 0.1% Oeq. and not with the material given by Zerilli and Armstrong [49], which has Oeq. ~1% and a yield stress at ambient temperature and 10^{-3} s^{-1} of 400 MPa. The interstitial content has a significant effect on the twinning stress, as discussed by Conrad et al. [51]. The rise in the twinning stress with interstitial content is more significant than the slip stress; this explains why the tendency for twinning decreases with interstitial increase. The effect of interstitials manifests itself in both the thermal and athermal components of the stress, and Conrad et al. [51] gives a value of $\Delta\tau = 0.02\ C_i^{1/2}$ at 300 K, where C_i is the atomic concentration of the interstitials.

3.2.4. Brasses

Fig. 7 shows the significant effect of the stacking-fault energy, γ, on the twinning stress for FCC metals. As an illustration of the effect of SFE on the incidence of twinning, the Cu–Zn system is analyzed. Gallagher [53] and Vöhringer [55,56] correlated the SFE to the e/a ratio in copper alloys and arrived at the following expression:

$$\ln \gamma = \ln \gamma_{Cu} + K_1\left(\frac{C/C_{max}}{1 + C/C_{max}}\right)^2 \quad (27)$$

where γ_{Cu} is the stacking fault energy for copper and C is the concentration of solute atoms. C_{max} is the maximum concentration of the solute. The best fit was

obtained with $K_1 = 12.5$; $\gamma_{Cu} = 57 \pm 8$ mJ/m^2. Eq. (27) can be combined with the mathematical representation of Fig. 7:

$$\sigma_T = K_2\left(\frac{\gamma}{Gb}\right)^{1/2} \tag{28}$$

A good fit is obtained with $K_2 = 6$ GPa. Substitution of Eq. (27) into Eq. (28) yields:

$$\sigma_T = \frac{K_2}{(Gb)^{1/2}}\exp\left[\ln \gamma_{Cu} + K_1\left(\frac{C/C_{max}}{1 + C/C_{max}}\right)^2\right]^{1/2} \tag{29}$$

The effect of solid solution (Zn, Ag, Al, Sn, Ge) atoms on the mechanical response of Cu has been established quite carefully; the effects of these solutes on the Hall–Petch equation has also been established. Vöhringer [13] proposed the following expression, which is used for the yield stress:

$$\sigma_S = \sigma_G + \sigma^* + k_S d^{1/2}$$
$$= \sigma_0 + K_3 \varepsilon_L^{4/3} C^{2/3} + \left[(\sigma^* + K_4 \varepsilon_L C^{2/3})\left(1 - \frac{k \ln \dot{\varepsilon}_0/\dot{\varepsilon}}{\Delta G_0}\right)^{1/p} T^{1/p}\right]^{1/q} + k_S d^{-1/2} \tag{30}$$

Eq. (30) is based on the overcoming of short-range obstacles, that have the shape dictated by the parameters p and q. The effect of the solid solution atoms is manifested (both in the thermal and athermal components of stress) through the $C^{2/3}$ relationship and the Labusch parameter ε_L, which has different values for different solid solution atoms. K_3 and K_4^*, are parameters, and ε_0 is a reference strain rate, that was taken by Vöhringer [13] as 10^{20} s^{-1}. This parameter is defined as:

$$\varepsilon_L = \sqrt{(\varepsilon_G)^2 + (\alpha \varepsilon_b)^2}$$

where

$$\varepsilon_G = \frac{1}{G}\frac{dG}{dc}$$

$$\varepsilon_b = \frac{1}{b}\frac{db}{dc}$$

ε_c expresses the effect of solute atoms on the shear modulus (G) and ε_b the effect on the Burgers vector (b). The parameter α was found to vary between 9 and 16 [60].

The effect of work hardening can be incorporated into Eq. (30) by adding the term $C_2\varepsilon''$ to the thermal component of stress.

The results of the calculations are represented in the slip–twinning transition plots of Fig. 9b, in which Eqs. (29) and (30) were used. These calculations were carried out for different Cu–Zn alloys: 5, 10, 15, and 20% at Zn, for a grain size of 50 μm. It is clear that the addition of Zn increases the propensity for twinning, displacing the slip–twinning transition upwards. By using Eq. (30) with the addition of the term $C_2\varepsilon''$ it is possible to establish the onset of twinning after different amounts of plastic deformation. Since Cu–Zn is FCC, the occurrence of twinning can occur after significant plastic deformation.

3.3. The Weertman–Ashby diagram

An immediate application of the constitutive description presented here is in the Weertman–Ashby deformation mechanism maps. In one of these maps, shown by Frost and Ashby [57], the axes are the strain rate and temperature; this type of plot is less common than the stress–temperature plot. It is directly applicable to the dynamic deformation of metals. As an illustration, Fig. 10 shows a map for titanium (G.S. = 100 μm). The original map had a domain called 'obstacle controlled plasticity'. The use of the constitutive equation described herein enabled the separation of this region into 'twinning' and 'slip' domains. The same procedure can be applied to any deformation-mechanism map, It should be emphasized that the calculated predictions presented in this section are not systematically compared with experimental results, since the emphasis of this report is on the methodology.

4. Grain size effects

Although considerable progress has been made in our understanding of the effect of grain size on the strength of metals, the early ideas of pile-ups, proposed by Hall [58], Petch [59], Cottrell [60], and reviewed by Armstrong [61], are still widely regarded as correct. Nevertheless, there are other effects of great importance. Four principal factors contribute to grain-boundary strengthening: (a) the grain boundaries act as barriers to plastic flow (the original pile-up mechanism [58–61]); (b) the grain boundaries act as dislocation sources [62]; (c) elastic anisotropy causes additional stresses in grain-boundary surroundings [66,67]; and (d) multislip is activated in the grain-boundary regions, whereas grain interiors are initially dominated by single slip, if properly oriented [65–68]. As a result, the regions adjoining grain boundaries harden at a rate much higher than grain interiors. A phenomenological constitutive equation predicting the effect of grain size on the yield stress of metals is discussed and extended to the nanocrystalline regime in Section 4.1. In Section 4.2, computational predictions are presented.

4.1. Analytical modeling

We present, in a succinct manner, the principal elements of a model proposed by Meyers and Ashworth

[67] and its recent application to the nanocrystalline [68]. A polycrystalline aggregate, upon being subjected to external tractions, develops a highly inhomogeneous state of internal stresses, due to the elastic anisotropy of the individual grains. Such inhomogeneous state of stress can only be avoided if the anisotropy ratio is one. For instance, for iron and copper, one has:

Fe	Cu
$E_{100} = 125$ GPa	$E_{100} = 67$ GPa
$E_{110} = 200$ GPa	$E_{110} = 130$ GPa
$E_{111} = 272$ GPa	$E_{111} = 190$ GPa

Fig. 11 shows polar plots of Young moduli for iron and copper. The effect of orientation on E is revealed in a striking manner. This is a well known but often ignored effect. This anisotropy generates additional stresses in the regions adjoining the grain boundaries. Plastic incompatibility [63,64] adds to the grain-boundary constraints. As a result, plastic deformation in the grain-boundary regions is more intense and involves a greater number of slip systems than the grain interiors. Fig. 12 shows a simplified schematic in which the grain-boundary regions show closer spaced slip bands and two operative slip systems, in contrast with the grain interiors, which are undergoing single slip. Mecking [72] developed the conceptual linkage of the various regions within a polycrystalline aggregate and there is a considerable experimental support for his concepts. Recently, Gray et al. [73] observed a higher dislocation density in the grain-boundary regions of plastically deformed brass, supporting the ideas discussed here. Meyers and Ashworth [67] considered the polycrystalline aggregate as a composite comprised of a grain interior with flow stress s_{fG}, and the grain boundary regions with flow stress s_{fGB}. They assigned a thickness t to the grain boundaries. The thickness t was assumed to vary with grain size D. The following functional dependence was taken:

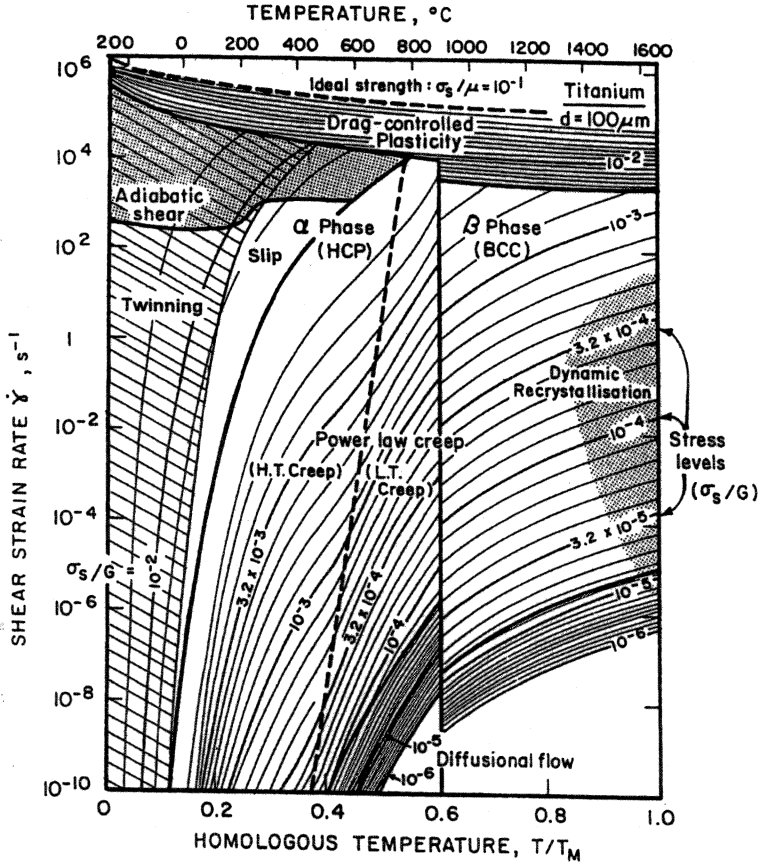

Fig. 10. Weertman–Ashby map for titanium (from Frost and Ashby [58], Fig. 17.4), $d = 100$ μm, in which a twinning domain has been inserted for 0.1% O_2 eq. titanium.

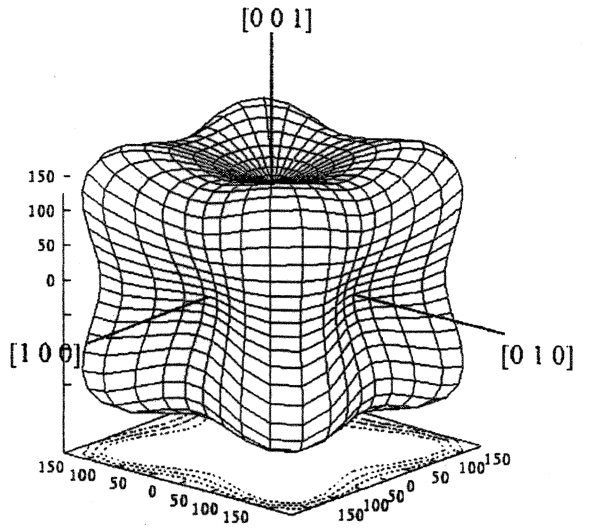

Fig. 11. Polar plots of E showing elastic anisotropy in (a) iron and (b) copper.

$$t = k_{MA} D^{1/2} \tag{31}$$

The rationale for this choice is as follows. A proportionality between t and D would lead to; $t = kD^1$. A fixed, grain-size insensitive t would yield; $t = kD^0$. The geometric mean provides the 1/2 exponent, necessary for the correct derivation, as will be seen below.

Substituting Eq. (31) into the composite equation, with some orientation considerations, leads to:

$$\sigma_y = \sigma_{fG} + 8k_{MA}(\sigma_{fGB} - \sigma_{fG})\bar{D}^{-1/2} - 16k_{MA}^2(\sigma_{fGB} - \sigma_{fG})\bar{D}^{-1} \tag{32}$$

For large grain sizes (the micrometer range) the $D^{-1/2}$ term dominates and a Hall–Petch relationship is obtained. The Hall–Petch slope, k_{HP}, is equal to:

$$k_{HP} = 8k_{MA}(\sigma_{fGB} - \sigma_{fG}) \tag{33}$$

As the grain size is decreased, the D^{-1} term becomes progressively dominant, and the σ_y versus $D^{-1/2}$ curve goes through a maximum. This occurs at:

$$D_c = (4k_{MA})^2 \tag{34}$$

For values of $D < D_c$, it is assumed that the flow stress reaches a plateau.

4.2. Comparison with experiments

The predictions of Eq. (32) are compared with the most extensive experimental results available in the literature, to the authors' knowledge. Yield stresses for nanocrystalline Fe and Cu, reported by Mallow and Koch [69,70], and Weertman et al. [71–74], respectively, are shown in Fig. 13. The experimental results in the nanocrystalline range are complemented by Hall–Petch slopes obtained by various investigators in the microcrystalline range. These slopes are reported in the literature. For iron, experimental results reported by Armstrong [58] were used. For copper, experimental results by Feltham and Meakin [75] and Andrade et al. [76] are used. There are other experimental results in the literature, that fall in the range reported in Fig. 13. For iron, Abrahamson [77] carried out experiments in the large grain size range of the conventional Hall–Petch plot and started to observe a deviation from the

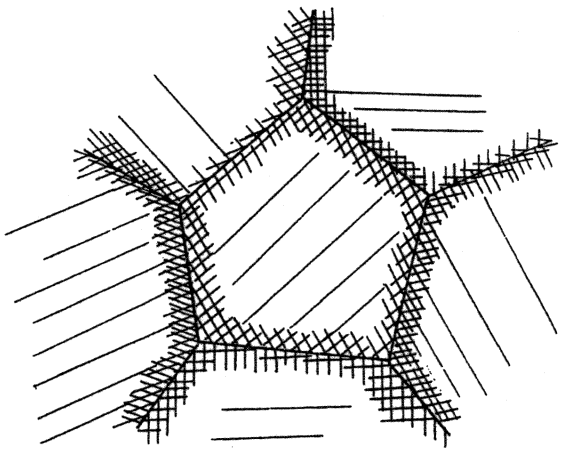

Fig. 12. Schematic configuration of slip in polycrystalline aggregate, at the first stage of plastic flow: notice activation of multiple slip in grain-boundary regions and single slip in grain interiors.

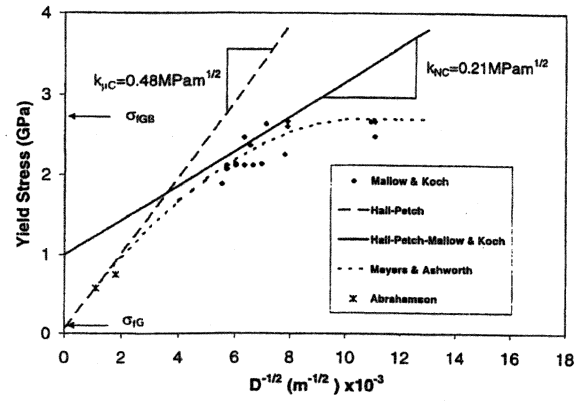

(a)

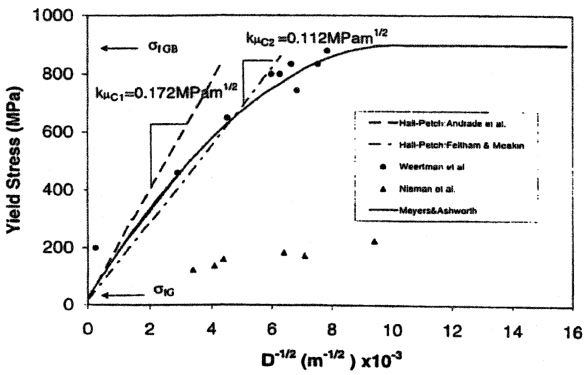

Fig. 13. σ_y versus $D^{-1/2}$ relationship for (a) iron and (b) copper; comparison of experimental results and predictions of Eq. (32).

Table 2
Parameters used for M–A equation

	σ_{fG} (MPa)	σ_{fGB} (MPa)	k_{HP} (MPa m$^{1/2}$)	k_{MA} (m$^{1/2}$)
Fe	100	2800	0.48	2.2×10^{-5}
Cu	25	900	0.112–0.172	$(1.6\text{–}2.4)\times10^{-5}$

accepted slope. Two experimental points from Abrahamson [77] are shown in Fig. 13a; the Hall–Petch slope starts to decrease.

It is clear, for both Fe and Cu, that the σ_y versus $D^{-1/2}$ relationship is not linear over the range millimeter–nanometer. The Hall–Petch line is an approximation that is effective in the mm–μm range. There is strong evidence that the slope decreases and that the curve asymptotically approaches a plateau when the grain size is progressively reduced. Eq. (32) is successful in representing the principal features observed experimentally. Three parameters have to be established: σ_{fG}, σ_{fGB}, and k_{MA}. σ_{fGB} is the saturation stress and represents the flow stress of the work hardened grain-boundary layer. It is taken as the maximum of the yield stress. k_{MA} is obtained by conversion of k_{HP} according to Eq. (33). This ensures a good match between HP and MA for large grain sizes. Table 2 shows the parameters used in the calculation. The curves in Fig. 13 represent the application of Eq. (32); a reasonable fit is obtained and the principal features are captured. For grain sizes below the maximum of the flow stress in the MA equation, a straight horizontal line is taken; in this regime, the grain boundaries (s_{fGB}) dominate the process.

The straight lines represent Hall–Petch fits. The slopes $k_{\mu C}$ represent Hall–Petch values taken from the literature for iron and copper. The line k_{nC} in Fig. 13a represents a Hall–Petch slope that is reported for the nanocrystalline regime. The slope in the nanocrystalline regime is obviously lower than in the microcrystalline regime. It is clear that there is a continuous variation in slope with grain size; thus, the Hall–Petch equation is a simplified representation valid in a limited range only.

There are many simplifications and assumptions in this model. The most prominent are:

1. The work hardened layer t is assumed to have a grain size dependence of $D^{-1/2}$. This assumption is based on the σ_y versus $D^{-1/2}$ dependence.
2. The flow stress of this layer is constant. In reality, a gradient of work hardening is expected.
3. The grain boundary flow stress reaches the saturation value σ_{fGB} at an early level of global plastic strain.

In spite of these drastic assumptions, a good fit is obtained and it is felt that the model captures the key physical features.

4.3. Computational predictions

For computational calculations, realistic polycrystal models were used and are shown in Fig. 14. Four grain sizes were modeled: 100, 10, 1, 0.1, and 0.05 μm (the latter not shown in Fig. 14). The thickness of the grain-boundary layer, t, was varied and the respective values shown in Fig. 14 are 3.75, 0.75, 0.15, and 0.03 μm. The microstructures, already divided into grain interiors and grain-boundary layers, are shown in Fig. 14. For the largest grain size modeled (100 μm), the grain-boundary region is barely distinguishable, whereas for the smallest grain size (0.1 μm), the grain-boundary region occupies a significant portion. The different mechanical responses of the two regions was also incorporated. The grain-boundary region was considered to undergo a rapid work hardening, expressed by a Voce equation, whereas the grain interiors were modeled as monocrystals.

The crystallographic orientation and specimen dimensions have a profound effect on the mechanical response of monocrystals. The different colors in Fig. 14 represent different possible crystallographic orienta-

tions. Three crystallographic orientations for the grain interiors were considered and they are shown in Fig. 15. The respective elastic moduli are also shown. Each grain was considered isotopic, but having its own Young's modulus. Efforts at implementing fully anisotropic response are underway. The monocrystal stress–strain response is taken from results reported by Diehl [78] and extended from a best fit with data for larger strains using results from Suzuki et al. [79]. The corresponding stress–strain curves, for the orientations C23, C26, and C30 are shown in Fig. 16a.

The rapidly work-hardening grain-boundary region was assumed to respond by a Voce equation with a saturation stress, s_s, equal to 900 MPa. Four curves are shown in Fig. 16b represent four work hardening rates. The curve with $e_r = 0.01$ was chosen for the computations. These two stress–strain responses were incorporated into the code Raven, developed by Benson [80,81] and calculations were successfully carried out. The results of one calculation for a grain size of 1 μm are shown in Fig. 17. The deformation sequence is shown for plastic strains of −0.009, −0.08, and −0.32. The plastic strains are higher in the grain interiors. As plastic deformation proceeds, the plastic strain in the grain interiors tends to form shear localized layers. It was possible to obtain stress–strain curves at various grain sizes and the results are reported in Fig. 18, together with the predictions of the Meyers–Ashworth equation. There is good correspondence between the two results and the decrease in the Hall Petch slope, as the grain size is decreased.

This confirms that elastic anisotropic effects, grain boundary sources, and the activation of two or more slip systems in polycrystals are responsible for the formation of a work hardened layer along the grain boundaries, early in the microplastic region. This grain boundary work-hardened layer becomes increasingly important as the grain size is decreased. Polycrystals are modeled (both analytically and computationally) as a composite of a work-hardened boundary layer surrounding grain interiors comprised of an annealed material having a essentially monocrystalline response.

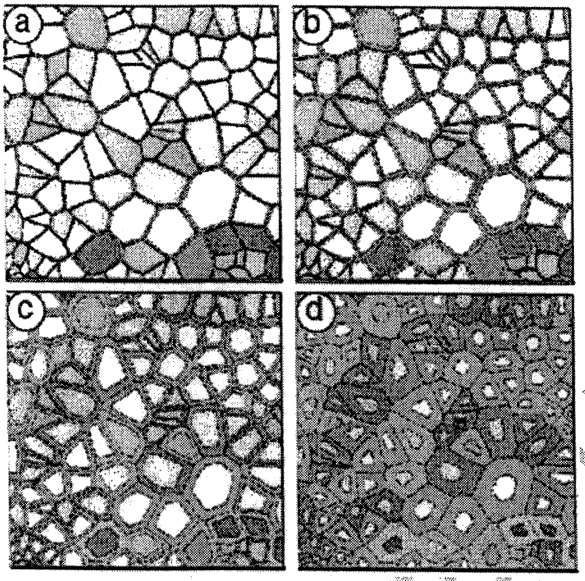

Fig. 14. Simulated polycrystalline aggregate used in computations; $D = 100$ μm, $t = 3.75$ μm; (b) $D = 10$ μm, $t = 0.75$ μm; (c) $D = 1$ μm, $t = 0.15$ μm; (d) $D = 0.1$ μm, $t = 0.03$ μm.

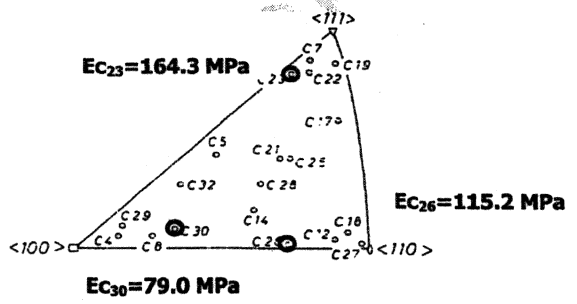

Fig. 15. Crystallographic orientation and equivalent Young modulus of crystalline (Adapted from Diehl [85]).

5. The upper limit: shock compression

We first report on recent experimental results on laser-induced shock compression experiments performed on copper single crystals with orientation [100] parallel to the shock front. These results, and the associated analysis, will be reported elsewhere in greater detail [82]. Copper has been the object of numerous shock recovery experiments and its response is fairly well understood. It has a stacking-fault energy of 57 ± 8 mJ/m^2. The shock-induced structure consists of dislocation cells; at higher pressures, beyond a critical threshold, twinning is prevalent. For single crystals, De Angelis and Cohen [83] found that the twinning stress was 14 GPa when the shock wave front was {100}, while it was 20 GPa when the orientation of the front was {111}. This is consistent with the findings by Nolder and Thomas [84,85] for nickel; they found a threshold of 35 GPa. As will be seen below, the results obtained generally confirm previous observations, albeit at a pulse duration that is lower by a factor of 1000 than that applied by Murr [86].

After shocking to 10 GPa, the copper crystals exhibited a cellular structure. Fig. 19a shows a characteristic region. The dislocation cell size is approximately 0.4 μm, consistent with the results by Murr [86]: 0.5 μm

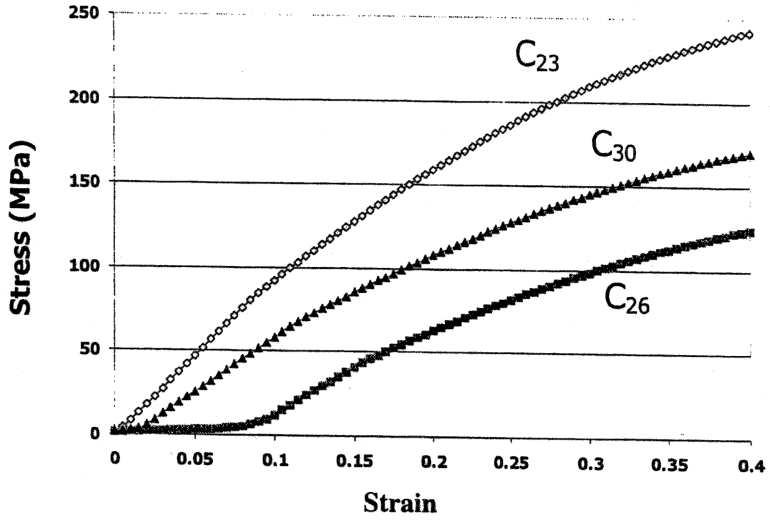

(a)

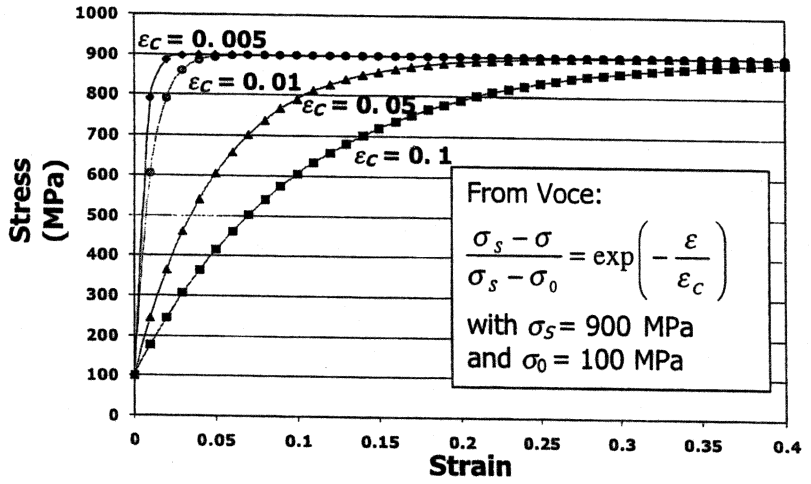

(b)

Fig. 16. (a) Plastic behavior of the grain interior: three grain orientations were taken from Diehl [78] curves; (b) grain-boundary region, modeled by Voce equation.

with 10 GPa and 0.3 μm with 15 GPa. They are also consistent with Gray's observations [87]: 0.5 μm with 10 GPa. However, the dislocation density, i.e. cell-wall thickness, seems to be lower than in these previous studies.

Increasing the pressure to 40 GPa revealed significantly different features, as shown in Fig. 19b. Perpendicular traces of planar features are seen when the beam direction is ⟨001⟩. These correspond to traces of {111} on (100). These traces have orientations ⟨220⟩. These traces are characteristic of stacking-fault bundles and twins and are analogous to previous observations by Murr [86], especially, Figs. 20–23 of Murr [86].

5.1. Prediction of dislocation densities

The observations made on recovered shock compressed copper specimens can be compared with analytical calculations that use physically-based mechanisms. Two aspects in particular can be predicted: the dislocation density as a function of peak shock amplitude and the threshold stress for twinning.

The first mechanism for shock induced dislocations is due to Smith [88]. It assumed an array of edge dislocations moving with the shock front. These dislocations played a role similar to epitaxial films: they accommodated the differences in lattice parameter. Hornbogen

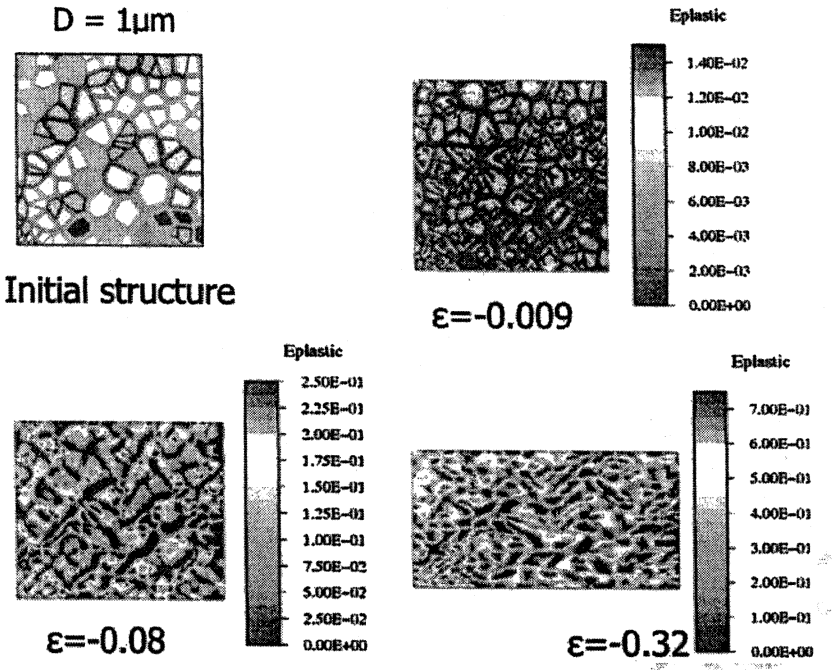

Fig. 17. Computation of plastic strains in 1-μm grain size specimen deformed to strains of −0.009, −0.08 −0.32; notice onset of shear localization (red bands).

[90] provided a significant improvement by considering edge and screw components of loops. He also considered the different mobilities of edge and screw components, determining the residual microstructure. A homogeneous dislocation nucleation mechanism [89] has been proposed by Meyers [90]. It assumed that dislocations are homogeneously generated at the front to accommodate the deviatoric stresses. In contrast with Smith's model, however, they are left behind. Weertman [91] proposed a mechanism for strong shocks using both a Smith interface and dislocations behind the front. The homogeneous dislocation generation mechanism is being improved by Meyers and Ravichandran [92] and is described here; a detailed account will appear somewhere else. The basic components of the model are reproduced here for clarity. Fig. 20 shows an idealized configuration of dislocations when a shock wave propagates through the lattice. The planes are (111) and the dislocations are edge dislocations. As the shock front advances, the dislocation interface is left behind. As this occurs, elastic deviatoric stresses build up. The initial calculations of resulting dislocation densities produced values orders of magnitude higher than the observed results [90]. An improved calculation, carried out by Meyers and Ravichandran [92], predicts values that compare favorably with dislocation densities measured from transmission electron microscopy observations. Fig. 20 shows several layers of interfacial dislocations that were generated and left behind the shock front. Not seen in this section are the screw components of the loops. The insertion of dislocations relaxes the deviatoric stresses that elastically distort an ideal cubic lattice to rhombohedral. Hence, a reduced cubic lattice is restored by the insertion of dislocations in the near vicinity of the interface. The dislocation spacing along the front required to accommodate this is d_2. This situation is analogous to the epitaxial growth of films, in which the disregistry is accommodated by interface dislocations, creating a semi-coherent boundary. The dislocation spacing along the front is calculated from the ratios of the original and compressed lattices. The initial and compressed

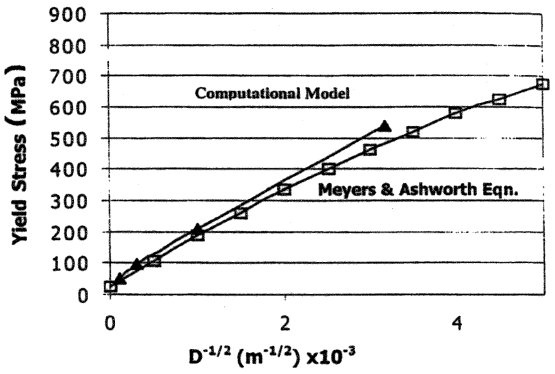

Fig. 18. Yield stress variation with grain size $D^{-1/2}$; notice decrease in slope at smaller grain sizes.

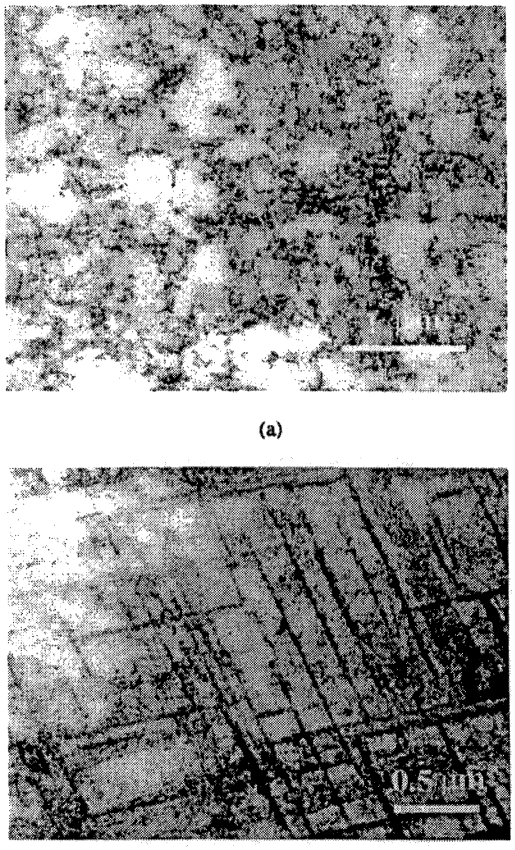

Fig. 19. Defect structures observed in copper monocrystal ([100] orientation) after laser-induced shock compression at (a) 10 GPa and (b) 40 GPa. Notice dislocation cell structure in (a) and twins/stacking faults in (b).

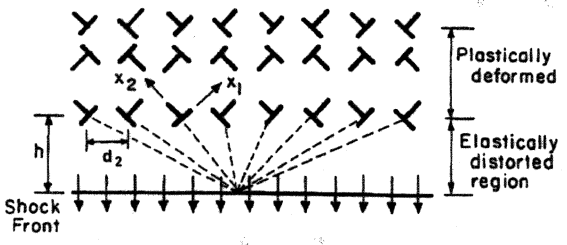

Fig. 20. Stress due to dislocations on a point at shock front.

specific volumes of the lattices being V and V_0, respectively, one has:

$$\left(\frac{V}{V_0}\right)^{1/3} = \frac{d_2 - d_1}{d_2} \tag{35}$$

d_1 is related to the Burgers vector by:

$$b\sqrt{2} = d_1 \tag{36}$$

The dislocation density generated can be calculated from d_2, the distance between dislocations at the front, and h, the spacing between successive dislocation loop layers nucleated. Since each distance d_2 corresponds to two dislocations [on planes (111) and (11-1)], the spacing $d_2/2$ is taken. Thus, the dislocation density, ρ, is:

$$\rho = \left(\frac{d_2 h}{2}\right)^{-1} \tag{37}$$

The spacing between dislocation loop layers can be calculated by using the stress fields around dislocations and summation at one point at the front over the stress field of all dislocations. This is shown in Fig. 20. Elastic distortion at the shock front is balanced by the stress fields due to the dislocation arrays. When the deviatoric elastic stresses at the front reach a critical level, dislocations are again generated. In order to calculate h, the superposition principle was applied and the total stress at a point on the front due to the dislocation array is estimated. Assuming edge dislocations only:

$$\sigma_{11} \sim \frac{Gb2\sqrt{2}}{2\pi(1-v)nd_2} \rightarrow \sum_{-\infty}^{\infty} \frac{1}{n} = 0 \tag{38}$$

$$\sigma_{22} \sim \frac{Gb}{2\pi(1-v)}(-2h^2)\frac{2\sqrt{2}}{n^3 d_2^3} \rightarrow \sum_{-\infty}^{\infty} \frac{1}{n^3} = 0 \tag{39}$$

$$\sigma_{12} \sim \frac{Gb}{2\pi(1-v)}\frac{2\sqrt{2h}}{n^2 d_2^2} \rightarrow \sum_{-\infty}^{\infty} \frac{1}{n^2} = \frac{\pi^4}{90} \tag{40}$$

where n is an integer designating the position of the dislocation ($n = -\infty \ldots \infty$). The series converge and lead to the estimate of the stresses.

Thus:

$$\sigma_{11} \sim 0 \quad \sigma_{22} \sim 0$$

$$\sigma_{12} \sim \frac{Gb}{\sqrt{2(1-v)}}\frac{\pi^3 h}{45 d_2^2} \tag{41}$$

When the stresses at the front reach a level at which homogeneous nucleation of dislocation loops can occur, then a new layer is formed. The dislocation density can be obtained from the stress for homogeneous nucleation of partial dislocation:

$$\frac{\sigma_{12}}{G} = 0.054 \tag{42}$$

Substituting Eq. (40) into Eq. (41):

$$h_1 = \frac{1-v}{b\pi^2} d_2^2 \tag{43}$$

for stationary dislocations. If the dislocation is assumed to move at the shear wave velocity, under the influence of the high residual shear stresses, they try to 'catch up' with the front. This results in an increase in h, given by the ratio between U_s, the shock velocity, and V_{sf}, the component of the shear wave velocity in the compressed medium. It will be assumed, to a first approxi-

mation, that the shock-wave velocity is equal to the longitudinal elastic wave velocity in an unbounded medium:

$$U_s \cong C_0 = \left(\frac{\lambda + 2\mu}{\rho_0}\right)^{1/2} \tag{44}$$

The dislocation velocity component along shock propagation direction is V_{dp}:

$$V_{dp} = \frac{\sqrt{2}}{2} C_s = \frac{1}{2}\left(\frac{2\mu}{\rho}\right)^{1/2} \tag{45}$$

where ρ_0 and ρ are the initial and compressed densities, respectively (equal to $1/V_0$ and $1/V$, respectively). Thus, for dislocations traveling at the shear wave velocity:

$$h_2 = h_1 \frac{C_0}{V_{dp}} = 2\left(\frac{1-v}{V_{sf}}\right)\left(\frac{V_0}{V}\right)^{1/2}\left(\frac{\lambda + 2\mu}{2\mu}\right)^{1/2} d_2^2 \tag{46}$$

The dislocation density as a function of V/V_0 is obtained by substituting Eq. (46) into Eq. (37) and Eqs. (35) and (36) into it:

$$\rho = \frac{1}{2b^2} = \left(\frac{\pi^2}{1-v}\right)\left\{\frac{V}{V_0}\left[1 - \left(\frac{V}{V_0}\right)^{1/3}\right]\right\}^3 \tag{47}$$

The dislocation density can be expressed as a function of pressure, P, through one of the equations obtained directly from the Rankine–Hugoniot equations and the equation of state [20]:

$$P = \frac{C_0^2(1 - (V/V_0))}{V_0[1 - S(1 - (V/V_0))]^2} \tag{48}$$

C_0 and S are the equation of state parameters specific to materials. Eq. (48) can be expressed as:

$$\frac{V}{V_0} = 1 - \frac{1}{2PV_0S^2}[2PV_0 + C_0 \pm \sqrt{(2PV_0 + C_0^2)^2 - 4P^2V_0^2S^2}] \tag{49}$$

If Eq. (49) is substituted into Eq. (47), the dislocation density is directly expressed as a function of pressure. Fig. 21a shows calculated dislocation densities for several metals: Cu, Ni, Fe, Ta, and Ti. The dislocation densities rise rapidly with increasing pressure and seem to reach a plateau (except for Ti). The significant differences in dislocation density observed for Fe and Ta, both BCC metals, can be attributed to differences in density and the shock parameter S; the significance of these differences is being evaluated. One should be careful in interpreting these results, since recovery processes occur at pressures much lower than the maximum in the plot, and these high dislocation densities are not reached. The predicted dislocation densities are plotted in Fig. 21b and compared with observations by Murr [81]. Two configurations are shown: dislocations moving at the shear wave velocity and stationary dislocations. For the latter case, we just use Eq. (43), which is substituted into Eqs. (35) and (37), and then into Eq. (48). This is given by Eq. (50):

$$P = \frac{C_0^2\{1 - \{1 - \sqrt{2}[(b^2(1-v)\rho)/2\pi^2]^{1/3}\}^3\}}{V_0\{1 - S\{1 - \sqrt{2}[(b^2(1-v)\rho)/2\pi^2]^{1/3}\}^3\}^2} \tag{50}$$

The results presented in Fig. 21b are encouraging, since the calculated densities 'bracket' the experimental results. This approach can lead to realistic prediction of dislocation densities.

5.2. Prediction of threshold amplitude for twinning

The methodology to be used in the prediction of the threshold shock amplitude for twinning was delineated by Murr et al. [93] and Meyers et al. [30]. The procedure presented herein can be used to predict the critical pressure for twinning in shock compression experiments. It is known that different metals have different threshold pressures for the initiation of twinning; it has been established by Murr [94] that this pressure is a function of stacking-fault energy, for FCC metals. Fig. 22 shows a normalized plot adapted from Murr [94]. The pressure was divided by the bulk modulus and the stacking-fault energy by the Gb product. The Murr plot (which assumes a linear relationship between P and γ, predicts, for instance, the critical twinning pressure for Al ($\gamma = 166$ mJ/m^2, $G = 26.1$ GPa, $b = 0.28$ nm). This value is $Pc/H = 0.5$ or $Pc = 38$ GPa. The twinning propensity is increased by decreasing the shock compression temperature and increasing the grain size. The following can be proposed to verify the correctness of this hypothesis: a shock compression experiment at 40 GPa, on an aluminum monocrystal with a [100] orientation at 77 K.

This methodology is extended and generalized here. Slip and twinning are considered as competing mechanisms; whereas plastic deformation by slip has a strain rate and temperature dependence well described by the theory of thermally-activated obstacles, it is assumed that the strain rate and temperature dependence for slip are much lower. This is corroborated by experimental evidence presented in Section 3. Setting $\sigma_T = \sigma_s$, one can obtain the critical twinning stress as a function of ε, $\dot{\varepsilon}$, and T. The application of this criterion to the shock front necessitates the knowledge of the strain rate. The strain rate at the shock front has been established by Swegle and Grady [95] to be:

$$P = k_{SG}\dot{\varepsilon}^{1/4} \tag{51}$$

Fig. 23 shows a Swegle–Grady plot in which the axes were normalized in order to provide a better superposition of data. The data has not entirely collapsed onto a single line, but the scatter is reduced. One could, to a first approximation, define a single k_{SG} parameter.

Two separate aspects have to be considered in the analysis: (a) shock heating and (b) plastic strain at the shock front. Both shock heating and plastic strain by slip (and associated work hardening) alter the flow stress of material by slip processes and need to be

incorporated into the computation. The total (elastic + plastic) uniaxial strain, e, at the shock front is related to the change in specific volume by:

$$\frac{V}{V_0} = e^{\varepsilon} \tag{52}$$

Inserting Eq. (52) into Eq. (48), we obtain:

$$P = \frac{C_0^2(1-e^{\varepsilon})}{V_0[1-S(1-e^{\varepsilon})]^2} \tag{53}$$

The shock temperature is a thermodynamic function of pressure [96]. It is represented by a fundamental formulation that uses the internal energy of the shocked material and convert it into heat through the heat capacity and density.

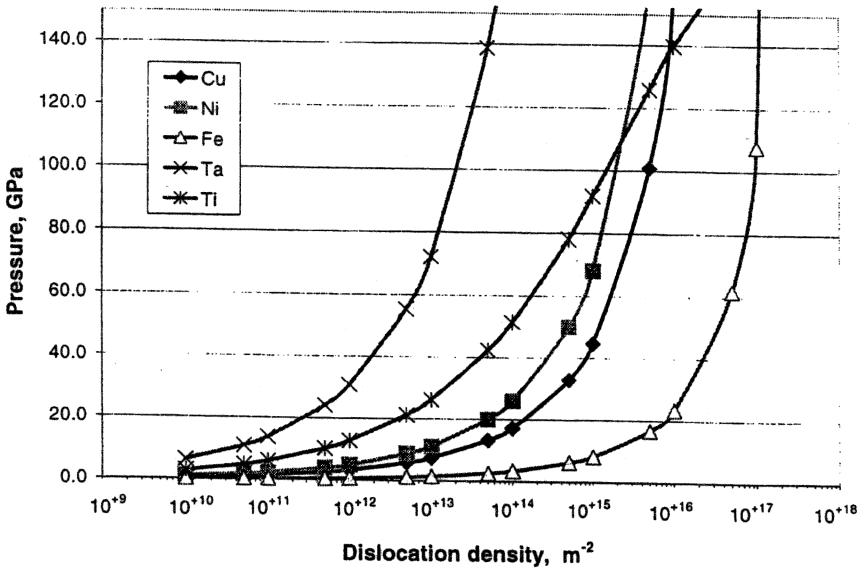

(a)

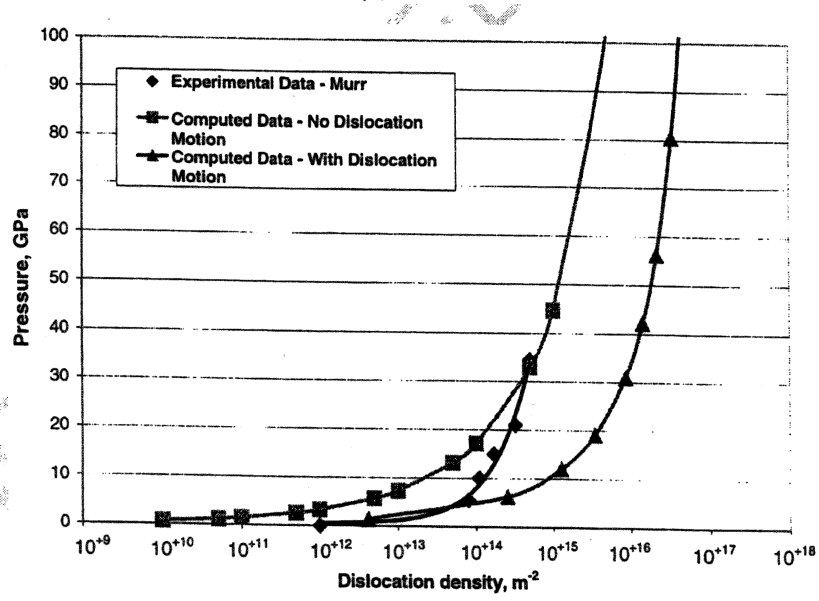

(b)

Fig. 21. (a) Calculated dislocation densities as a function of pressure for representative metals; (b) experimental and computed results for shock compression of copper.

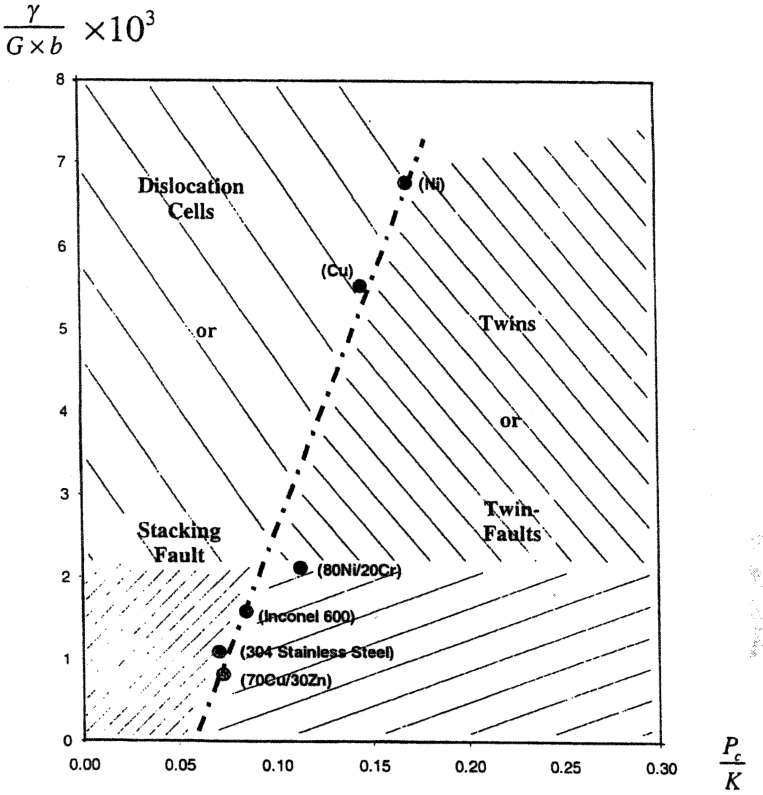

Fig. 22. Normalized pressure/stacking fault energy plot showing twinning and dislocation domains (adapted from Murr [94]).

$$T=\frac{(V_0-V)}{2C_v}P + \frac{\exp[(-\gamma_0/V_0)V]}{2C_v}\int_{V_0}^{V} P\cdot\exp[(\gamma_0/V_0)V]\left[2-\left(\frac{\gamma_0}{V_0}\right)(V_0-V)\right]dV \quad (54)$$

The constitutive response of the copper monocrystal is represented by the modified MTS expression below; the parameters are taken from Follansbee and Gray [98]. The MTS equation is obtained from Eq. (15), with values of $p=1/2$ and $q=3/2$, respectively [97]. The value of g_0 is 0.8 [98].

$$\sigma=\sigma_0 f(\varepsilon)\left[1-\left(\frac{kT}{Gb^3g_0}\ln\left(\frac{\dot{\varepsilon}_0}{\dot{\varepsilon}}\right)\right)^{2/3}\right]^2 \quad (55)$$

The work hardening (f(e)) was incorporated by taking a polynomial representation of the stress strain curve shown for orientation C30 in Fig. 16a. This orientation is the closest to [100], which has the lowest threshold pressure for twinning. This polynomial is:

$$f(\varepsilon) = 45\,510\varepsilon^6 - 86\,899\varepsilon^5 + 63\,406\varepsilon^4 - 21\,834\varepsilon^3 + 2901.8\varepsilon^1 - 1.92 \quad (56)$$

The grain size effects were incorporated by adding a Hall–Petch term to Eq. (55)

The procedure used in calculating the threshold stress is to first obtain the threshold stress through Eqs. (22) and (24), and Eq. (51). The value of this stress is then used to calculate the shock strain and temperature through Eqs. (53) and (54), respectively. These values are then fed back into Eqs. (22) and (24) and Eq. (51)

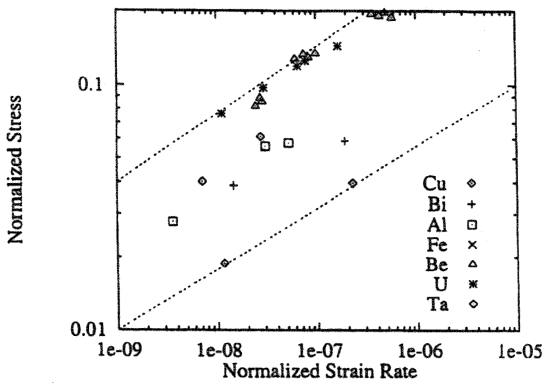

Fig. 23. Modified Swegle–Grady plot with normalized axes (Adapted from Swegle and Grady [95]).

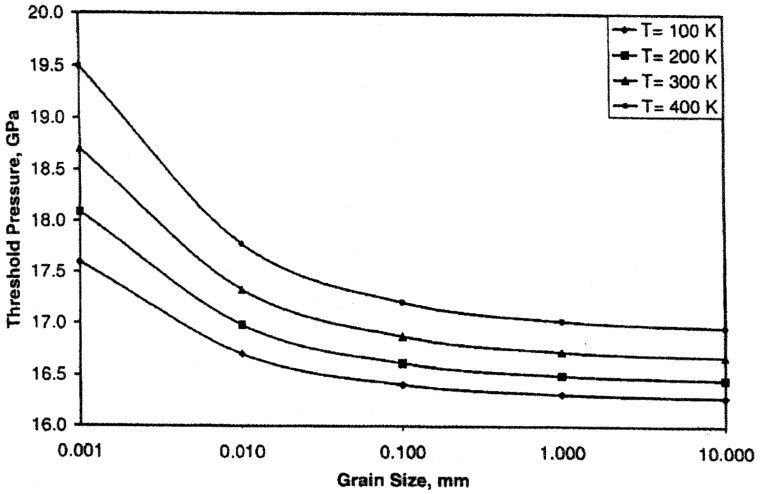

Fig. 24. Threshold shock pressure for twinning in copper as a function of grain size at different initial temperatures (100, 200, 300 and 400 K).

and a second pressure is calculated. This iterative process converges to the critical twinning stress. Fig. 24 shows the application of this method to copper. The plot shows how the initial temperature and grain size affect the threshold shock pressure. There is a significant increase in the threshold stress when the grain size is decreased from 10 mm to 1 m. The shock temperature has a small effect on the threshold pressure. The calculated thereshold pressure for a monocrystal (modeled by a 10-mm grain size) shocked from an initial temperature of 300 K is 17 GPa. This compares favorably with experimental results by De Angelis and Cohen [83]: 14 GPa. This approach, which was not optimized here, yielded results that are close to actual observations. They represent the first prediction of twinning threshold in shock compression. It is expected that in the near future we will be able to predict the effect of other microstructural parameters, such as the stacking-fault energy, especially the twinning threshold, and substructures generated in shock compression.

6. Conclusions

We presented, in Sections 2–5, four interrelated research lines in which we apply or develop constitutive descriptions for predicting the mechanical behavior of metals. The following aspects were investigated: (a) instability (Section 2); (b) the slip–twinning transition(-Section 3); (c) grain-size effects (Section 4); and (d) shock compression (Section 5). The rapid development and dissemination of computational capabilities increases significantly the usefulness of these constitutive equations and guides the evolution of research themes. The quantitative treatment of mechanical response of metals is evolving into accurate constitutive equations. The constitutive description is moving away from phenomenological equations toward physically-based equations, as the computational capabilities increase.

The following principal phenomena and effects are currently captured:

- work hardening/softening;
- thermal softening;
- strain rate effects;
- grain size effects;
- texture effects;
- creep;
- pressure dependence; and
- fracture.

Efforts are underway to incorporate the following effects into codes:

- dynamic recovery and recrystallization;
- dynamic strain aging;
- twinning;
- alloying effects; and
- environmental effects.

It is the feeling of the authors that physically-based constitutive equations, incorporating a greater and greater complexity of the physics of deformation and damage, will evolve in the near future. It behooves us Materials Scientists and Engineers to transform our intuitive 'feel' into quantitative analyses that can be effectively implemented into large-scale computations.

Acknowledgements

This research was supported by the US Army Research Office Multidisciplinary University Research Initiative (Contract No. DAAH 04-96-1-0376), by the Department of Energy (Grants DEFG0398DP00212 and DEFG0300SF2202), and by the National Science

Foundation (Grant DMI-9612017). The help of Mr Sebastien Tillay (Ecole Centrale de Nantes) and of Mr Randy Pohle in calculations is greatly appreciated, as are numerous discussions with Prof. G. Ravichandran (California Institute of Technology). The collaboration with Drs Bruce Remington and Daniel Kalantar (Lawrence Livermore National Laboratory) and with the OMEGA ICF (U. of Rochester) staff is greatly appreciated. The copper specimens were shock loaded at that facility through the kind work of Dr D. Kalantar and Dr T. Boehly. The transmission electron microscopy was carried out in collaboration with Dr Fabienne Gregori, U. of Paris.

References

[1] R.L. Orr, O.D. Sherby, J.E. Dorn, Trans. ASM 46 (1954) 113.
[2] A.K. Mukherjee, J.E. Bird, J.E. Dorn, Trans. ASM 62 (1964) 155.
[3] R. Becker, Z. Phys. 26 (1925) 919.
[4] A. Seeger, Z. Naturf. 9A (1954) 758.
[5] A. Seeger, Z. Naturf. 9A (1954) 818.
[6] A. Seeger, Z. Naturf. 9A (1954) 851.
[7] A. Seeger, in: S. Flugge (Ed.), Handbuch der Physik, VII/1, Springer, 1955, p. 383.
[8] H. Conrad, H. Wiedersich, Acta Met. 8 (1960) 128.
[9] H. Conrad, J. Met. 16 (1964) 582.
[10] H. Conrad, Mater. Sci. Eng. 6 (1970) 265.
[11] A.S. Krausz, H. Eyring, Deformation Kinetics, Wiley, NY, 1975.
[12] K. Ono, Appl J. Phys. 39 (1968) 1803.
[13] O. Vöhringer, Die Strukturmechanischen Grundlagen der Plastischen Verformung von Vielkristallinen-Kupfer-Legierungen, Habilitationsschrift, Karlsruhe, 1972.
[14] U.F. Kocks, A.S. Argon, M.F. Ashby, Thermodynamics and Kinetics of Slip, Prog. Mater. Sci, vol. 19, Pergamon Press, Oxford, 1975.
[15] P.S. Follansbee, U.F. Kocks, Acta Met. 36 (1988) 81.
[16] J.R. Klepaczko, Mater. Sci. Eng. 18 (1975) 121.
[17] J.R. Klepaczko, Impact Loading and Dynamic Behavior of Materials, DGM, Germany, 1988, p. 823.
[18] F.J. Zerilli, R.W. Armstrong, J. Appl. Phys. 61 (1987) 1816.
[19] F.J. Zerilli, R.W. Armstrong, J. Appl. Phys. 68 (1990) 915.
[20] M.A. Meyers, Dynamic Behavior of Materials, J. Wiley, NY, 1994, p. 362.
[21] M.A. Meyers, in: M.A. Meyers, R.W. Armstrong, H.O.K. Kirchner (Eds.), Mechanics and Materials, J. Wiley, 1999, p. 489.
[22] J.H. Bechtold, Acta Met. (1955) 249–254.
[23] K.G. Hoge, A.K. Mukherjee, J. Mat. Sci. 12 (1977) 1666–1672.
[24] T.E. Mitchell, W.A. Spitzig, Acta Met. 13 (1965) 1169–1179.
[25] M.A. Meyers, Y.-J. Chen, F.D.S. Marquis, D.S. Kim, Met. Mat. Trans. A 26A (1995) 2493.
[26] Y.J. Chen, M.A. Meyers, V.F. Nesterenko, Mater. Sci. Eng. A268 (1999) 70.
[27] C.L. Wittman, C.M. Lopatin, J.P. Swensen, T.J. Holmquist, in: R. Asfahani, E. Chen, A. Crowson (Eds.), High Strain Rate Behavior of Refractory Metals and Alloys, TMS-AIME, Warrendale, PA, 1992, pp. 167–178.
[28] F.J. Zerilli, R.W. Armstrong, J. Phys. IV France 7 (1997) C3637-42.
[29] L.E. Murr, M.A. Meyers, C.-S. Niou, Y.-J. Chen, S. Pappu, C.S. Kennedy, Acta Mat. 45 (1997) 157.
[30] M.A. Meyers, O. Vöhringer, Y.-J. Chen, in: S. Ankem, C.S. Pande (Eds.), Advances in Twinning, TMS-AIME, Warrendale, PA, 1999, p. 43.
[31] M.A. Meyers, O. Vöhringer, unpublished results (2000).
[32] J.W. Christian, S. Mahajan, Prog. Mater. Sci. 39 (1995) 1.
[33] S. Mahajan, D.F. Williams, Intl. Met. Rev. 18 (1973) 43.
[34] R.E. Reed-Hill, J.P. Hirth, and H.C. Rogers (Eds.), Deformation Twinning, Gordon and Breach, NY, 1964.
[35] R.E. Reed-Hill, Inhomogeneity of Plastic Deformation, ASM, Metals Park, OH, 1973, p. 285.
[36] J. Harding, Mem. Sci. Rev. Met. 65 (1968) 245.
[37] J. Harding, Proc. R. Soc. 299A (1967) 464.
[38] R.W. Armstrong, P.J. Worthington, A constitutive relation for deformation twinning in body centered cubic metals, in: R.W. Rohde, B.M. Butcher, J.R. Holland, C.H. Karnes (Eds.), Metallurgical Effects at High Strain Rates, Plenum, NY, 1973, p. 294.
[39] O. Vöhringer, Z. Metallkunde 67 (1976) 51.
[40] O. Vöhringer, Z. Metallkunde 65 (1974) 352.
[41] J.A. Venables, Phil. Mag. 6 (1961) 379.
[42] S. Asgari, E. El-Danaf, S.R. Kalidindi, R.D. Doherty, Met. Mat. Trans. 28A (1997) 1781.
[43] E. El-Danaf, S.R. Kalidindi, R.D. Doherty, Met. Mat. Trans. A 30A (1999) 1223.
[44] G.T. Gray, III, G.C. Kaschner, T.A. Mason, P.J. Maudlin, S.R. Chen, in: S. Ankem, C.S. Pande (Eds.), Advances in Twinning, TMS-AIME, Warrendale, PA, 1999, p. 157.
[45] W.G. Johnston, J.J. Gilman, J. Appl. Phys. 30 (1959) 129.
[46] D.F. Stein, Jr., J.R. Low, J. Appl. Phys. 31 (1960) 362–369.
[47] P.R. Thornton, T.E. Mitchell, Phil. Mag. 7 (1962) 361.
[48] J.J. Gilman, Phil. Mag. 76 (1997) 329.
[49] F.J. Zerilli, R.W. Armstrong, J. Appl. Phys. 61 (1987) 1816.
[50] F.J. Zerilli, R.W. Armstrong, in: S.C. Schmidt, W.C. Tao (Eds.), Shock Compression of Condensed Matter-1995, AIP, Woodbury, NY, 1996, p. 315.
[51] F.J. Zerilli, R.W. Armstrong, Grain size and mechanical properties — fundamentals and applications, in: MRS Symposium Proceedings, vol. 362, MRS, Pittsburgh, 1995, p. 149.
[52] G.T. Gray, III, J. Phys. 4 (7) (1997) C3–423.
[53] H. Conrad, M. Doner, B. de Meester, in: R.I. Jaffee, H.M. Burte (Eds.), Titanium Science and Technology, Plenum, NY, 1973, pp. 969–1004.
[54] K. Okazaki, H. Conrad, Acta Met. 21 (1973) 1117.
[55] O. Vöhringer, Metall 11 (1972) 1119.
[56] R. Labusch, Phys. Stat. Sol. 41 (1970) 159.
[57] H.J. Frost, M.F. Ashby, Deformation-Mechanism Maps, Pergamon Press, Oxford, 1982.
[58] E.O. Hall, Proc. R. Soc. (Lond.) B64 (1951) 474.
[59] N.J. Petch, J. Iron Steel Inst. 174 (1953) 25.
[60] A.H. Cottrell, Trans. TMS-AIME 212 (1958) 192.
[61] R.W. Armstrong, in: R.F. Bunshah (Ed.), Advances in Materials Research, vol. 5, Wiley-Interscience, NY, 1971, p. 101.
[62] J.C.M. Li, Trans. TMS-AIME 227 (1963) 75.
[63] M.F. Ashby, Phil. Mag. 21 (1970) 399.
[64] J.P. Hirth, Met. Trans. 3 (1972) 61.
[65] A.W. Thompson, in: A.W. Thompson (Ed.), Work Hardening in Tension and Fatigue, AIME, 1977, p. 399.
[66] H. Margolin, M.S. Stanescu, Acta Met. 23 (1975) 1141.
[67] M.A. Meyers, E. Ashworth, Phil. Mag., A 46 (1982) 737.
[68] D.J. Benson, M.A. Meyers, H.-H. Fu, Mater. Sci. Eng. in press (2000).
[69] J.C. Suits, B. Chalmers, Acta Met. 12 (1961) 854.
[70] P.J. Worthington, E. Smith, Acta Met. 12 (1964) 1277.
[71] L.E. Murr, S.S. Hecker, Scr. Met. 13 (1979) 667.
[72] Mecking, in: N. Hansen, A. Horsewell, T. Leffers, and H. Lilholt (Eds.), Deformation of Polycrystals: Mechanisms and Microstructures, Riso Natl. Lab. Denmark, 1981, pp. 73–86.

[73] G.T. Gray, III, H.R. Chen, K.S. Vecchio, Met. Mat. Trans. A 30A (1999) 1235.
[74] T.R. Mallow, C.C. Koch, Acta Mat. 45 (1997) 2177.
[75] Feltham, J.D. Meakin, Phil. Mag. 2 (1957) 105.
[76] M.A. Meyers, U.R. de Andrade, A.H. Chokshi, Met Mat. Trans. 26A (1995) 2881.
[77] E.P. Abrahamson, II, Surfaces and Interfaces, Syracuse Univ. Press, 1968, p. 262.
[78] J. Diehl, Z. Metallk. 47 (1956) 33.
[79] H. Suzuki, T. Ikeda, T. Takeuchi, J. Phys. Soc. Jpn. 11 (1956) 382.
[80] D.J. Benson, Comp. Meth. Appl. Mech. Eng. 999 (1992) 235.
[81] B. van Leer, J. Comp. Phys. 23 (1977) 276.
[82] M.A. Meyers, F. Gregori, B.K. Kad, D.H. Kalantar, B.A. Remington, J.S. Wark, T. Boehly, Plastic Deformation in Laser-Induced Shock Compression of Monocrystalline Copper, in preparation (2000).
[83] R.J. De Angelis, J.B. Cohen, J. Metals 15 (1963) 681.
[84] R.L. Nolder, G. Thomas, Acta Met. 11 (1963) 994.
[85] R.L. Nolder, G. Thomas, Acta Met. 12 (1964) 227.
[86] L.E. Murr, in: M.A. Meyers, L.E. Murr (Eds.), Shock Waves and High-Strain-Rate Phenomena in Metals, Plenum, NY, 1981, p. 607.
[87] G.T. Gray, in: M.A. Meyers, L.E. Murr, K.P. Staudhammer (Eds.), Shock-Wave and High-Strain-Rate Phenomena in Materials, M. Dekker, NY, 1992, p. 899.
[88] C.S. Smith, Trans. AIME 212 (1958) 574.
[89] E. Hornbogen, Acta Met. 10 (1962) 978.
[90] M.A. Meyers, Scr. Met. 12 (1978) 21.
[91] J. Weertman, Mech. Mater. 5 (1986) 13.
[92] M.A. Meyers, G. Ravichandran, unpublished results (2000).
[93] L.E. Murr, M.A. Meyers, C-S. Niou, Y-J. Chen, S. Pappu, C. Kennedy, Acta Mater. 45 (1997) 157–175.
[94] L.E. Murr, in: S.C. Schmidt, N.C. Holmes (Eds.), Shock Waves in Condensed Matter, Elsevier, Amsterdam, 1988, p. 315.
[95] J.W. Swegle, D.E. Grady, J. Appl. Phys. 58 (1983) 941.
[96] M.A. Meyers, Dynamic Behavior of Materials, J. Wiley, NY, 1994, p. 149.
[97] P.S. Follansbee, in: L.E. Murr, K.P. Staudhammer, M.A. Meyers, M. Dekker (Eds.), Metallurgical Applications of Shock-Wave and High-Strain Rate Phenomena, 1986, p. 451.
[98] P.S. Follansbee, G.T. Gray, III, Mater. Sci. Eng. 138 (1991) 23.